# Convergence and conditioning of a Nyström method for Stokes flow in exterior three-dimensional domains

**J. Li · O. Gonzalez**

**Abstract** Convergence and conditioning results are presented for the lowest-order member of a family of Nyström methods for arbitrary, exterior, three-dimensional Stokes flow. The flow problem is formulated in terms of a recently introduced two-parameter, weakly singular boundary integral equation of the second kind. In contrast to methods based on product integration, coordinate transformation and singularity subtraction, the family of Nyström methods considered here is based on a local polynomial correction determined by an auxiliary system of moment equations. The polynomial correction is designed to remove the weak singularity in the integral equation and provide control over the approximation error. Here we focus attention on the lowest-order method of the family, whose implementation is especially simple. We outline a convergence theorem for this method and illustrate it with various numerical examples. Our examples show that well-conditioned, accurate approximations can be obtained with reasonable meshes for a range of different geometries.

**Keywords** Stokes equations, boundary integral equations, single-layer potentials, double-layer potentials, Nyström approximation

**Mathematics Subject Classification (2010)** 65N38, 76D07, 31B10

## 1 Introduction

We consider the problem of determining the slow, steady flow of an incompressible viscous fluid past a moving body of arbitrary shape. Mathematically, the problem is described by the classic Stokes system in an exterior, three-dimensional domain with prescribed velocity data. This problem plays a central role in the study of hydrodynamic convection and diffusion processes for small particles in dilute solution, specifically in the determination of convection and diffusion coefficients,

J. Li, Graduate Program in Computational and Applied Mathematics, The University of Texas, Austin, (Current address: Schlumberger Corporation, Houston, TX), E-mail: JLi49@slb.com · O. Gonzalez, Department of Mathematics, The University of Texas, Austin, E-mail: og@math.utexas.edu

which have numerous practical and theoretical applications. On the practical side, such coefficients play a central role in the design of mass transfer equipment used in various biochemical industries. On the theoretical side, such coefficients play a central role in various experimental methods in physical chemistry [17, 60, 63], which are used to measure and study the structural properties of molecules like proteins and DNA [1–5, 14, 25, 27]. A detailed understanding of the convective and diffusive properties of particles in solution is fundamental in many different applications, ranging from sequencing technologies for DNA [42, 45, 46], to the design of a variety of microfluidic devices in physics, chemistry and biology [12, 13, 19–21, 34, 55, 57–59, 62]. Indeed, the interplay between diffusion and convection is crucially important in the design and performance of devices for the transport, mixing, separation and manipulation of particles.

Several approaches are available for the analysis and numerical treatment of the exterior Stokes problem. Due to the unbounded character of the domain, boundary integral approaches are generally preferable over domain approaches. For instance, the numerical treatment of the latter requires special considerations such as domain truncation and artificial boundary conditions. Within the class of boundary integral approaches, it is well-known that a formulation based on either of the classic single- or double-layer Stokes potentials is inadequate or incomplete [53, 54]; each formulation alone is not capable of representing an arbitrary exterior flow. However, various authors have shown that a double-layer formulation can be modified in different ways to obtain completeness [31, 35, 40, 50, 52]. Here we employ a completed double-layer formulation of Stokes flow recently studied in [26]. This formulation combines the strengths of various previous approaches and is natural for bodies of complicated shape and topology. The formulation is a weakly singular boundary integral equation of the second kind, involves two free parameters, and has been shown to be uniquely solvable for arbitrary exterior flows under minimal regularity assumptions consistent with classic potential theory [30, 47]; specifically, that the boundary is a Lyapunov surface of class $C^{1,1}$ and that the velocity data is of class $C^0$.

In this article, we study a Nyström method for approximating the complete, weakly singular boundary integral formulation of exterior Stokes flow introduced in [26]. We introduce a general family of methods, and then outline a convergence result for the lowest-order method in the family under minimal regularity assumptions as above. In contrast to methods based on product integration [10, 36], coordinate transformation [15, 64] and singularity subtraction [8, 37, 56], the family of Nyström methods described here is based on a local polynomial correction determined by an auxiliary system of moment equations. The polynomial correction is designed to remove the weak singularity in the integral equation and provide control over the approximation error. Moreover, for the method considered here, there are no weakly singular integrals that need to be evaluated. We outline a theorem which shows that the lowest-order method is convergent on $C^{1,1}$ Lyapunov surfaces with $C^0$ data, and that the convergence rate is at least linear under higher regularity assumptions. Surfaces with this minimal regularity arise naturally in various applications, for example in molecular modeling. As a corollary of our result, a simple singularity subtraction method which has been employed by many authors is implied to be convergent under the same assumptions.

We present numerical experiments on several different geometries that illustrate both the convergence and the conditioning of the method as a function of

the free parameters in the boundary integral formulation. Our experiments show that high accuracy can be achieved on reasonable meshes for a range of different geometries, including some with rather high curvatures. Moreover, our experiments show that the associated linear systems are well-conditioned for a large range of parameter values independent of the level of mesh refinement. Consequently, these systems can be solved efficiently using iterative methods without pre-conditioners. We remark that several types of Galerkin and collocation methods [10,11,18,36] could also be considered, as well as spectral Galerkin [9,23,29] and wavelet-based methods [6,41,61]. However, these approaches generally require basis functions that may be difficult to construct, or which may exist only for certain classes of geometries. Moreover, they require special techniques for computing weakly singular integrals, which can be expensive. Our results show that the lowest-order member of a family of locally-corrected Nyström methods provides a simple, efficient and provably convergent alternative to these and various other higher-order methods. Indeed, for boundary surfaces and data of limited regularity, the lowest-order method introduced here may achieve a comparable rate of convergence without the extra cost.

The mathematical theory of convergence of Nyström methods for boundary integral equations of the second kind on regular surfaces is a well-studied subject. The convergence theory for standard methods on problems with continuous kernels is classic [10,24,36]. Similarly, the theory for product integration methods on problems with weakly singular kernels is also well-established [10,24,36], although some of the hypotheses may be difficult to verify in three-dimensional problems. Convergence results for methods based on floating polar coordinate transformations are described in [15,38,64]. Convergence results for methods based on the classic idea of singularity subtraction as introduced by Kantorovich and Krylov [37] have been established for one-dimensional problems in [8], and have been studied for higher-dimensional problems in [56]. Locally-corrected methods based on auxiliary moment equations were considered in [16], but no mathematical convergence results were given. Here we introduce a family of locally-corrected methods for the vector-valued Stokes problem in three-dimensions and outline a convergence result for the lowest-order method. Detailed proofs for the entire family of methods for a general class of boundary integral equations are given in a separate work [28].
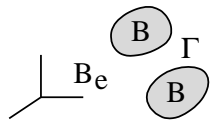
The presentation is structured as follows. In Section 2 we outline the Stokes equations for the steady flow of an incompressible viscous fluid in an exterior domain. In Section 3 we establish notation and outline the properties of the classic surface potentials for the Stokes equations that will be needed throughout our developments. In Section 4 we summarize the two-parameter boundary integral formulation of Stokes flow to be approximated. In Section 5 we introduce the Nyström approximation and outline our convergence result, and in Section 6 we present our numerical experiments.

## 2 The exterior Stokes problem

Here we define the boundary value problem to be studied. We briefly outline standard assumptions which guarantee existence and uniqueness of solutions, and introduce various flow quantities of interest that will arise in our analysis. For further details on the exterior Stokes problem see [40].

## 2.1 Formulation

We consider the steady motion of a body of arbitrary shape through an incompressible viscous fluid at low Reynolds number. In a body-fixed frame, we denote the body domain by $B$, the fluid domain exterior to the body by $B_e$, and the body-fluid interface by $\Gamma$. Given a body velocity field $v : \Gamma \to \mathbb{R}^3$, the basic problem is to find a fluid velocity field $u : B_e \to \mathbb{R}^3$ and pressure field $p : B_e \to \mathbb{R}$ which satisfy the classic Stokes equations, which in non-dimensional form are

$$
\begin{aligned}
u_{i,jj} - p_{,i} &= 0, \ x \in B_e \\
u_{i,i} &= 0, && x \in B_e \\
u_i &= v_i, && x \in \Gamma \\
u_i, p &\to 0, && |x| \to \infty.
\end{aligned}
\tag{1}
$$

Equation $(1)_1$ is the local balance law of linear momentum for the fluid and $(1)_2$ is the local incompressibility constraint. Equation $(1)_3$ is the no-slip boundary condition which states that the fluid and the body velocities coincide at each point of the boundary. The limits in $(1)_4$ are boundary conditions which are consistent with the fluid being at rest at infinity. Unless mentioned otherwise, all vector quantities are referred to a single basis and indices take values from one to three. Here and throughout we use the usual conventions that a pair of repeated indices implies summation, and that indices appearing after a comma denote partial derivatives.

## 2.2 Solvability

We assume $B \cup \Gamma \cup B_e$ fills all of three-dimensional space, $B$ is open and bounded, and $B_e$ is open and connected. Moreover, we assume $\Gamma$ consists of a finite number of disjoint, closed, bounded and orientable components, each of which is a Lyapunov surface [30]. These conditions on $\Gamma$ imply that standard results from potential theory for the Stokes equations may be applied [40,50,53]. Moreover, together with the continuity of $v$, they are sufficient to guarantee that (1) has a unique solution $(u, p)$ among fields with the following decay properties [22,33,40]:

$$
u_i = O(|x|^{-1}), \quad u_{i,j} = O(|x|^{-2}), \quad p = O(|x|^{-2}) \quad \text{as} \quad |x| \to \infty.
\tag{2}
$$

The solution $(u, p)$ is smooth in $B_e$, but may possess only a finite number of bounded derivatives in $B_e \cup \Gamma$ depending on the precise smoothness of $\Gamma$ and $v$.

## 2.3 Basic flow quantities

The volume flow rate associated with a flow $(u, p)$ and a given oriented surface $S$ is defined by

$$
Q = \int_S u_i(x) n_i(x) \, dA_x,
\tag{3}
$$

where $n : S \to \mathbb{R}^3$ is a given unit normal field and $dA_x$ denotes an infinitesimal area element at $x \in S$. When $S$ is closed and bounded, we always choose $n$ to be the outward unit normal field. In this case, $Q$ quantifies the volume expansion rate of the domain enclosed by $S$.

The fluid stress field associated with a flow $(u, p)$ is a function $\sigma : B_e \to \mathbb{R}^{3 \times 3}$ defined by

$$\sigma_{ij} = -p\delta_{ij} + u_{i,j} + u_{j,i}, \tag{4}$$

where $\delta_{ij}$ is the standard Kronecker delta symbol. For each $x \in B_e$ the stress tensor $\sigma$ is symmetric in the sense that $\sigma_{ij} = \sigma_{ji}$. The traction field $f : S \to \mathbb{R}^3$ exerted by the fluid on a given oriented surface $S$ is defined by

$$f_i = \sigma_{ij} n_j. \tag{5}$$

The resultant force $F$ and torque $T$, about an arbitrary point $c$, associated with $f$ are

$$F_i = \int_S f_i(x) \, dA_x, \qquad T_i = \int_S \varepsilon_{ijk}(x_j - c_j) f_k(x) \, dA_x, \tag{6}$$

where $\varepsilon_{ijk}$ is the standard permutation symbol. As before, when $S$ is closed and bounded, we always choose $n$ to be the outward unit normal field. In this case, $F$ and $T$ are loads exerted on $S$ by the fluid exterior to $S$.

For convenience, we assume all quantities have been non-dimensionalized using a characteristic length scale $\ell > 0$, velocity scale $\vartheta > 0$ and force scale $\mu\vartheta\ell > 0$, where $\mu$ is the absolute viscosity of the fluid. The dimensional quantities corresponding to $\{x, u, p, v\}$ are $\{\ell x, \vartheta u, \mu\vartheta\ell^{-1}p, \vartheta v\}$, and the dimensional quantities corresponding to $\{Q, \sigma, f, F, T\}$ are $\{\vartheta\ell^2 Q, \mu\vartheta\ell^{-1}\sigma, \mu\vartheta\ell^{-1}f, \mu\vartheta\ell F, \mu\vartheta\ell^2 T\}$.

## 3 Surface potentials for the Stokes equations

In this section we outline the classic single- and double-layer surface potentials for the Stokes equations, summarize their main properties, and establish notation that will be needed in our developments. For further details on the mathematical properties of these potentials see [32].

### 3.1 Definition

Let $\psi : \Gamma \to \mathbb{R}^3$ be a given function, which we assume to be continuous unless mentioned otherwise. Then by the Stokes single-layer potentials on $\Gamma$ with density $\psi$ we mean

$$\begin{aligned} V_i[\Gamma, \psi](x) &= \int_\Gamma U_{ij}^{\mathrm{PF}}(x, y)\psi_j(y) \, dA_y \\ P_V[\Gamma, \psi](x) &= \int_\Gamma \Pi_j^{\mathrm{PF}}(x, y)\psi_j(y) \, dA_y, \end{aligned} \tag{7}$$

and by the Stokes double-layer potentials on $\Gamma$ with density $\psi$ we mean

$$\begin{aligned} W_i[\Gamma, \psi](x) &= \int_\Gamma U_{ijl}^{\mathrm{STR}}(x, y)\psi_j(y)\nu_l(y) \, dA_y \\ P_W[\Gamma, \psi](x) &= \int_\Gamma \Pi_{jl}^{\mathrm{STR}}(x, y)\psi_j(y)\nu_l(y) \, dA_y. \end{aligned} \tag{8}$$

Here $(U_{ij}^{\mathrm{PF}}, \Pi_j^{\mathrm{PF}})$ and $(U_{ijl}^{\mathrm{STR}}, \Pi_{jl}^{\mathrm{STR}})$ are the classic stokeslet (or point-force) and stresslet solutions of the free-space Stokes equations with pole at $y$ [26,54], and

$\nu$ is the unit normal field on $\Gamma$ directed outwardly from $B$. Using the notation $z = x - y$ and $r = |z|$, explicit expressions for the stokeslet and stresslet solutions are

$$U_{ij}^{\mathrm{PF}} = \frac{\delta_{ij}}{r} + \frac{z_i z_j}{r^3}, \quad \Pi_j^{\mathrm{PF}} = \frac{2z_j}{r^3} \tag{9}$$

$$U_{ijl}^{\mathrm{STR}} = \frac{3z_i z_j z_l}{r^5}, \quad \Pi_{jl}^{\mathrm{STR}} = -\frac{2\delta_{jl}}{r^3} + \frac{6z_j z_l}{r^5}. \tag{10}$$

We remark that, due to the linearity of the free-space equations, the above solutions are defined up to an arbitrary choice of normalization. The choice of normalization naturally affects various constants in the developments that follow, but is not crucial in any way; the choice adopted here is taken from [26]. While we only consider the Stokes potentials with densities in the classic spaces of continuous functions, they could also be considered on various Sobolev spaces [32].

3.2 Analytic properties

For arbitrary density $\psi$ the single-layer potentials $(V[\Gamma, \psi], P_V[\Gamma, \psi])$ and double-layer potentials $(W[\Gamma, \psi], P_W[\Gamma, \psi])$ are smooth at each $x \notin \Gamma$. Moreover, by virtue of their definitions as continuous linear combinations of stokeslets and stresslets, they satisfy the homogeneous Stokes equations $(1)_{1,2,4}$ at each $x \notin \Gamma$.

For arbitrary $\psi$ the functions $V[\Gamma, \psi]$ and $W[\Gamma, \psi]$ are well-defined for all $x \in B \cup \Gamma \cup B_e$. For $x \in \Gamma$ the integrands in $(7)_1$ and $(8)_1$ are unbounded functions of $y \in \Gamma$, but the integrals exist as improper integrals in the usual sense [30] provided that $\Gamma$ is a Lyapunov surface. The restrictions of $V[\psi, \Gamma]$ and $W[\psi, \Gamma]$ to $\Gamma$ are denoted by $\overline{V}[\psi, \Gamma]$ and $\overline{W}[\psi, \Gamma]$. These restrictions are continuous functions on $\Gamma$ [40]. Moreover, for any $x_0 \in \Gamma$ the following limit relations hold [40, 53, 54]:

$$\lim_{\substack{x \to x_0 \\ x \in B_e}} V[\Gamma, \psi](x) = \overline{V}[\Gamma, \psi](x_0) \tag{11}$$

$$\lim_{\substack{x \to x_0 \\ x \in B}} V[\Gamma, \psi](x) = \overline{V}[\Gamma, \psi](x_0) \tag{12}$$

$$\lim_{\substack{x \to x_0 \\ x \in B_e}} W[\Gamma, \psi](x) = \quad 2\pi\psi(x_0) + \overline{W}[\Gamma, \psi](x_0) \tag{13}$$

$$\lim_{\substack{x \to x_0 \\ x \in B}} W[\Gamma, \psi](x) = -2\pi\psi(x_0) + \overline{W}[\Gamma, \psi](x_0). \tag{14}$$

Notice that, by continuity of $\psi$ and $\overline{W}[\Gamma, \psi]$, the one-sided limits in (13) and (14) are themselves continuous functions on $\Gamma$.

In contrast to the case with $V[\Gamma, \psi]$ and $W[\Gamma, \psi]$, for arbitrary $\psi$ the functions $P_V[\Gamma, \psi]$ and $P_W[\Gamma, \psi]$ do not exist as improper integrals in the usual sense when $x \in \Gamma$. In particular, the integrands in $(7)_2$ and $(8)_2$ are excessively singular functions of $y \in \Gamma$. Nevertheless, for sufficiently smooth $\Gamma$ and $\psi$, the functions $P_V[\Gamma, \psi]$ and $P_W[\Gamma, \psi]$ have well-defined limits as $x$ approaches the surface $\Gamma$ [40, 53, 64]. Directly-defined values of $P_V[\Gamma, \psi]$ and $P_W[\Gamma, \psi]$ on $\Gamma$ may be obtained by appealing to the theory of singular and hyper-singular integrals [44, 48, 49].

3.3 Associated stress fields

For arbitrary density $\psi$ the stress fields associated with the single- and double-layer potentials are

$$\Sigma_V^{ik}[\Gamma,\psi](x) = \int_\Gamma \Xi_{ikj}^{\text{PF}}(x,y)\psi_j(y)\,dA_y \tag{15}$$

$$\Sigma_W^{ik}[\Gamma,\psi](x) = \int_\Gamma \Xi_{ikjl}^{\text{STR}}(x,y)\psi_j(y)\nu_l(y)\,dA_y, \tag{16}$$

where $\Xi_{ikj}^{\text{PF}}$ and $\Xi_{ikjl}^{\text{STR}}$ are the stress functions corresponding to the stokeslet and stresslet solutions in (9) and (10). In particular, we have [26,54]

$$\Xi_{ikj}^{\text{PF}} = -\frac{6z_i z_k z_j}{r^5}, \tag{17}$$

$$\Xi_{ikjl}^{\text{STR}} = \frac{2\delta_{ik}\delta_{jl}}{r^3} + \frac{3(\delta_{ij}z_k z_l + \delta_{il}z_j z_k + \delta_{jk}z_i z_l + \delta_{lk}z_i z_j)}{r^5} - \frac{30 z_i z_j z_k z_l}{r^7}. \tag{18}$$

For arbitrary $\psi$ the single-layer stress field $\Sigma_V[\Gamma,\psi]$ is smooth at each $x \notin \Gamma$ and is the actual stress field associated with the Stokes flow with velocity field $V[\Gamma,\psi]$ and pressure field $P_V[\Gamma,\psi]$. A similar remark applies to the double-layer stress field $\Sigma_W[\Gamma,\psi]$. For $x \in \Gamma$ and arbitrary $\psi$ the single-layer traction field $\Sigma_V[\Gamma,\psi]\nu$ exists as an improper integral in the usual sense, but not the double-layer traction field $\Sigma_W[\Gamma,\psi]\nu$. Moreover, for sufficiently smooth $\Gamma$ and $\psi$ the following limit relations for $\Sigma_V[\Gamma,\psi]\nu$ [40,53] and $\Sigma_W[\Gamma,\psi]\nu$ [53] hold for each $x_0 \in \Gamma$, where we use the notation $x_\epsilon = x_0 + \epsilon\nu(x_0)$:

$$\lim_{\substack{\epsilon\to 0 \\ \epsilon>0}} \Sigma_V[\Gamma,\psi](x_\epsilon)\nu(x_0) = -4\pi\psi(x_0) + \Sigma_V[\Gamma,\psi](x_0)\nu(x_0) \tag{19}$$

$$\lim_{\substack{\epsilon\to 0 \\ \epsilon<0}} \Sigma_V[\Gamma,\psi](x_\epsilon)\nu(x_0) = \quad 4\pi\psi(x_0) + \Sigma_V[\Gamma,\psi](x_0)\nu(x_0) \tag{20}$$

$$\lim_{\substack{\epsilon\to 0 \\ \epsilon>0}} \Sigma_W[\Gamma,\psi](x_\epsilon)\nu(x_0) = \lim_{\substack{\epsilon\to 0 \\ \epsilon<0}} \Sigma_W[\Gamma,\psi](x_\epsilon)\nu(x_0). \tag{21}$$

The result in (21) is commonly referred to as the Lyapunov-Tauber condition. A directly-defined value of $\Sigma_W[\Gamma,\psi]\nu$ on $\Gamma$ may be obtained by appealing to the theory of hyper-singular integrals [44,48,49].

3.4 Flow properties

Let $S$ be an arbitrary closed, bounded surface which encloses $\Gamma$ in its interior domain and let $n$ be the outward unit normal field on $S$. For arbitrary $\psi$ the resultant force $F_V[\Gamma,\psi]$, torque $T_V[\Gamma,\psi]$ about an arbitrary point $c$, and volume flow rate $Q_V[\Gamma,\psi]$ associated with $S$ and the single-layer flow $(V[\Gamma,\psi], P_V[\Gamma,\psi])$ are [26]

$$F_V[\Gamma,\psi] = \int_S \Sigma_V[\Gamma,\psi](x)n(x)\,dA_x = -8\pi\int_\Gamma \psi(y)\,dA_y \tag{22}$$

$$T_V[\Gamma,\psi] = \int_S (x-c)\times\Sigma_V[\Gamma,\psi](x)n(x)\,dA_x = -8\pi\int_\Gamma (y-c)\times\psi(y)\,dA_y \tag{23}$$

$$Q_V[\Gamma,\psi] = \int_S V[\Gamma,\psi](x)\cdot n(x)\,dA_x = 0. \tag{24}$$

Because the above results hold for any $S$ which encloses $\Gamma$, we can pass to the limit and conclude that the resultant force, torque, and volume flow rate associated with $\Gamma$ and the exterior single-layer flow are also given by these results.

Similar calculations can be performed in the double-layer case. For arbitrary $\psi$ the resultant force $F_W[\Gamma, \psi]$, torque $T_W[\Gamma, \psi]$ about an arbitrary point $c$, and volume flow rate $Q_W[\Gamma, \psi]$ associated with $S$ and the flow $(W[\Gamma, \psi], P_W[\Gamma, \psi])$ are [26]

$$F_W[\Gamma, \psi] = \int_S \Sigma_W[\Gamma, \psi](x) n(x) \, dA_x = 0 \tag{25}$$

$$T_W[\Gamma, \psi] = \int_S (x - c) \times \Sigma_W[\Gamma, \psi](x) n(x) \, dA_x = 0 \tag{26}$$

$$Q_W[\Gamma, \psi] = \int_S W[\Gamma, \psi](x) \cdot n(x) \, dA_x = 4\pi \int_\Gamma \psi(y) \cdot \nu(y) \, dA_y. \tag{27}$$
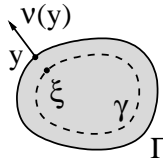
As before, because the above results hold for any $S$ which encloses $\Gamma$, we can pass to the limit and conclude that the resultant force, torque, and volume flow rate associated with $\Gamma$ and the exterior double-layer flow are also given by these results.

## 4 Boundary integral formulation

Here we outline the two-parameter boundary integral formulation of (1) that is to be approximated, briefly summarize its main properties, and state a fundamental existence and solvability result.

### 4.1 Formulation

Let $\gamma$ be a surface parallel to $\Gamma$ offset towards $B$ by a distance $\phi \geq 0$. In particular, $\gamma$ is the image of the map $\xi = \vartheta(y) : \Gamma \to \mathbb{R}^3$ defined by



$$\xi = y - \phi \nu(y). \tag{28}$$

By virtue of the fact that $\Gamma$ is a Lyapunov surface it follows that the map $\vartheta : \Gamma \to \gamma$ is continuous and one-to-one for all $\phi \in [0, \phi_\Gamma)$, where $\phi_\Gamma$ is a positive constant. In the absence of any global obstructions, we have $\phi_\Gamma = 1/\kappa_\Gamma$, where $\kappa_\Gamma$ is the maximum of the signed principal curvatures of $\Gamma$ [51]. Here we use the convention that curvature is positive when $\Gamma$ curves away from its outward unit normal $\nu$. As a consequence, the principal curvatures are the eigenvalues of the gradient of $\nu$ (not $-\nu$) restricted to the tangent plane. From the geometry of parallel surfaces we have the following relations for all $y \in \Gamma$, $\xi = \vartheta(y) \in \gamma$ and $\phi \in [0, \phi_\Gamma)$ [51]:

$$n(\xi) = \nu(y), \quad dA_\xi = J^\phi(y) dA_y, \quad J^\phi(y) = 1 - 2\phi \kappa^m(y) + \phi^2 \kappa^g(y). \tag{29}$$

Here $n$ is the outward unit normal on $\gamma$, $dA_\xi$ and $dA_y$ are area elements on $\gamma$ and $\Gamma$, and $\kappa^m$ and $\kappa^g$ are the mean and Gaussian curvatures of $\Gamma$. For $\phi \in [0, \phi_\Gamma)$

we denote the inverse of $\xi = \vartheta(y)$ by $y = \varphi(\xi)$. In view of (28) and $(29)_1$ we have $y = \xi + \phi n(\xi)$.

Given an arbitrary density $\psi : \Gamma \to \mathbb{R}^3$ and number $\theta \in [0,1]$ define $u : B_e \to \mathbb{R}^3$ and $p : B_e \to \mathbb{R}$ by

$$u = \theta V[\gamma, \psi \circ \varphi] + (1 - \theta)W[\Gamma, \psi], \qquad p = \theta P_V[\gamma, \psi \circ \varphi] + (1 - \theta)P_W[\Gamma, \psi]. \quad (30)$$

Notice that the double-layer potentials are defined on the surface $\Gamma$ with density $\psi$, while the single-layer potentials are defined on the parallel surface $\gamma$ with density $\psi \circ \varphi$. In particular, the two types of potentials are defined on different surfaces, but involve only one arbitrary density.

By properties of the single- and double-layer potentials, the fields $(u, p)$ are smooth at each $x \in B_e$ and satisfy the Stokes equations $(1)_{1,2,4}$ at each $x \in B_e$. The stress field $\sigma : B_e \to \mathbb{R}^{3 \times 3}$ associated with $(u, p)$ is given by

$$\sigma = \theta \Sigma_V[\gamma, \psi \circ \varphi] + (1 - \theta)\Sigma_W[\Gamma, \psi], \quad (31)$$

and the resultant force $F$, torque $T$ about an arbitrary point $c$, and volume flow rate $Q$ associated with $\Gamma$ are

$$F = \theta F_V[\gamma, \psi \circ \varphi], \quad T = \theta T_V[\gamma, \psi \circ \varphi], \quad Q = (1 - \theta)Q_W[\Gamma, \psi]. \quad (32)$$

Here we have used linearity and the flow properties of the single- and double-layer potentials outlined in Section 3.4.

In order that $(u, p)$ provide the unique solution of the exterior Stokes boundary-value problem (1), the boundary condition $(1)_3$ must be satisfied. In particular, given $v : \Gamma \to \mathbb{R}^3$, we require

$$\lim_{\substack{x \to x_0 \\ x \in B_e}} u(x) = v(x_0), \qquad \forall x_0 \in \Gamma. \quad (33)$$

Substituting for $u$ from (30) and using the limit relation in (13) we obtain a boundary integral equation for the unknown density $\psi$:

$$\theta V[\gamma, \psi \circ \varphi](x_0) + (1 - \theta)\overline{W}[\Gamma, \psi](x_0) + 2\pi(1 - \theta)\psi(x_0) = v(x_0), \quad \forall x_0 \in \Gamma. \quad (34)$$

From this we can deduce that $(u, p)$ defined in (30) will be the unique solution of (1) if and only if $\psi$ satisfies (34). By definition of the single- and double-layer potentials, this equation can be written in integral form as

$$\theta \int_\gamma U_{ij}^{\mathrm{PF}}(x, \xi)\psi_j(\varphi(\xi))\, dA_\xi \\ + \ (1 - \theta) \int_\Gamma U_{ijl}^{\mathrm{STR}}(x, y)\psi_j(y)\nu_l(y)\, dA_y \\ + \ 2\pi(1 - \theta)\psi_i(x) = v_i(x), \quad \forall x \in \Gamma, \quad (35)$$

where $x_0$ has been replaced by $x$ for convenience. By performing a change of variable in the first integral this equation can then be put into the operator form

$$\mathcal{G}^{\theta, \phi}\psi + \mathcal{H}^\theta\psi + c^\theta\psi = v, \quad (36)$$

where $c^\theta = 2\pi(1 - \theta)$ and

$$(\mathcal{G}^{\theta, \phi}\psi)(x) = \int_\Gamma G^{\theta, \phi}(x, y)\psi(y)\, dA_y, \quad G_{ij}^{\theta, \phi}(x, y) = \theta J^\phi(y)U_{ij}^{\mathrm{PF}}(x, \vartheta(y)), \quad (37)$$

and

$$(\mathcal{H}^\theta\psi)(x) = \int_\Gamma H^\theta(x, y)\psi(y)\, dA_y, \quad H_{ij}^\theta(x, y) = (1 - \theta)U_{ijl}^{\mathrm{STR}}(x, y)\nu_l(y). \quad (38)$$

4.2 Solvability theorem

The following result establishes the solvability of the integral equation (36), equivalently, (34). Its proof is given in [26].

**Theorem 1** *There exists a unique solution $\psi \in C^0$ of the boundary integral equation (36) for any closed, bounded Lyapunov surface $\Gamma \in C^{1,1}$, parallel offset parameter $\phi \in [0, \phi_\Gamma)$, interpolation parameter $\theta \in (0, 1)$ and boundary data $v \in C^0$.*

The above result implies that the representation in (30) is complete and stable for any $\theta \in (0, 1)$ and $\phi \in [0, \phi_\Gamma)$. It is complete because arbitrary solutions of the exterior Stokes boundary-value problem (1) can be represented in the form (30) with a unique density $\psi$ for each $\theta$ and $\phi$. It is stable because it leads to a uniquely solvable Fredholm equation of the second kind. In particular, for each $\theta$ and $\phi$, the linear operator in (36) has a finite condition number and the density $\psi$ depends continuously on the data $v$. The smoothness properties of $\psi$ depend on those of the surface $\Gamma$ and the data $v$.

Various limiting cases of the formulation are well-understood. For arbitrary $\phi \in [0, \phi_\Gamma)$, the case with $\theta = 0$ in (30) corresponds to a pure double-layer representation of $(u, p)$. It is well-known that such a representation is incomplete in the sense that it can represent only those flows for which the resultant force and torque on $\Gamma$ vanish, that is, $F = 0$ and $T = 0$ [40, 50, 53, 54]. Equivalently, the range of the linear operator in (36) is deficient, leading to solvability conditions and non-uniqueness for $\psi$. For arbitrary $\phi \in [0, \phi_\Gamma)$, the case with $\theta = 1$ in (30) corresponds to a pure single-layer representation of $(u, p)$. It is well-known that such a representation is also incomplete in the sense that it can represent only those flows for which the volumetric expansion rate of $\Gamma$ vanishes, that is, $Q = 0$ [40, 50, 53, 54]. Equivalently, the range of the linear operator in (36) is again deficient, leading to solvability conditions and non-uniqueness for $\psi$. For arbitrary $\theta \in (0, 1)$, the single-layer operator is weakly singular when $\phi = 0$ and non-singular or regular when $\phi > 0$. Moreover, various degeneracies can occur in the limit $\phi \to \phi_\Gamma$ depending on $\Gamma$, for example the area of the parallel surface, and consequently the single-layer potential, may vanish in this limit.

Aside from the restriction of solvability, the parameters $\theta$ and $\phi$ are arbitrary and can be exploited. For example, they might be chosen to optimize the condition number of the linear operator in (36). While this condition number is finite for all $\theta \in (0, 1)$ and $\phi \in [0, \phi_\Gamma)$, it becomes unbounded as $\theta \to 0$ and $\theta \to 1$ because the limiting operators have non-trivial null spaces as discussed above. Moreover, depending on $\Gamma$, it may also become unbounded as $\phi \to \phi_\Gamma$ because the parallel surface may vanish, or other types of degeneracies may occur; roughly speaking, the larger the value of $\phi$, the more difficult it may be for the single-layer operator on the parallel surface to complete the range of the double-layer operator on the original surface. Based on these considerations, it is reasonable to expect that optimal conditioning might occur near the point $(\theta, \phi) = (1/2, 0)$. This expectation will be confirmed by our numerical experiments which show that the formulation is indeed rather well-conditioned for a wide range of parameter values near this point. In our developments below, we restrict attention to the regularized case with $\phi > 0$. As we will see, a simple and efficient numerical method which does not require the treatment of weakly singular integrals can be constructed for this regularized case, which is a main motivation for considering it.

**5 Locally-corrected Nyström approximation**

In this section we describe a numerical method for the boundary integral equation (36). We introduce a general family of locally-corrected Nyström methods, and then present solvability and convergence results for the lowest-order method in the family under minimal regularity assumptions consistent with classic potential theory [30, 47].

5.1 Mesh, quadrature rule

We consider an arbitrary decomposition of $\Gamma$ into non-overlapping quadrature elements $\Gamma^e$, $e = 1, \ldots, E$, each with area $|\Gamma^e| > 0$. To any such decomposition we associate a size parameter $h = \max_e(\operatorname{diam}(\Gamma^e)) > 0$. For simplicity, we assume that the elements are either all quadrilateral or all triangular. In our analysis, we consider sequences of decompositions with increasing $E$, or equivalently, decreasing $h$. We will only consider sequences that satisfy a uniform refinement condition in the sense that the area of all elements is reduced at the same rate. Specifically, we assume

$$Ch^2 \le |\Gamma^e| \le C'h^2, \quad \forall e = 1, \ldots, E, \quad E \ge E_0. \tag{A1}$$

Here $C$, $C'$ and $E_0$ are positive constants whose values may change from one appearance to the next.

In each element $\Gamma^e$, we introduce quadrature nodes $x_q^e$ and weights $W_q^e > 0$, $q = 1, \ldots, Q$, where $Q$ is independent of $e$, such that

$$\int_\Gamma f(x)\, dA_x = \sum_{e=1}^E \int_{\Gamma^e} f(x)\, dA_x \approx \sum_{e=1}^E \sum_{q=1}^Q f(x_q^e) W_q^e. \tag{39}$$

We assume that the quadrature nodes and weights are defined by mapping each element $\Gamma^e$ to a standard, planar domain using a local parameterization, and applying a local quadrature rule in the standard domain. In this case, the Jacobian of the parameterization would be included in the weights $W_q^e$. We assume that the quadrature weights remain bounded and that the quadrature points remain distinct and in the element interiors. Specifically, for any sequence of decompositions that satisfy the uniform refinement condition, we assume

$$Ch^2 \le \sum_{q=1}^Q W_q^e \le C'h^2, \quad \forall e = 1, \ldots, E, \quad E \ge E_0,$$
$$Ch \le \operatorname{dist}(x_q^e, \partial\Gamma^e) \le h, \quad \forall q = 1, \ldots, Q, \quad e = 1, \ldots, E, \quad E \ge E_0,$$
$$Ch \le \min_{(e,q)\ne(e',q')} |x_q^e - x_{q'}^{e'}| \le h, \quad \forall q, q' = 1, \ldots, Q, \quad e, e' = 1, \ldots, E, \quad E \ge E_0.$$
$$\tag{A2}$$

To quantify the error in a quadrature rule for a given function $f$ on a given surface $\Gamma$, we introduce the normalized local truncation errors

$$\tau(e, f, h) = \frac{1}{|\Gamma^e|} \left| \int_{\Gamma^e} f(x)\, dA_x - \sum_{q=1}^Q f(x_q^e) W_q^e \right|, \quad e = 1, \ldots, E. \tag{40}$$

For sequences of decompositions that satisfy a uniform refinement condition, we require that the above truncation errors vanish uniformly in $e$ depending on properties of $f$. Specifically, we assume there exists an integer $\ell \geq 1$ such that

$$\max_e \ \tau(e, f, h) \to 0 \text{ as } h \to 0 \text{ for each } f \in C^0,$$
$$\max_e \ \tau(e, f, h) \leq Ch^\ell \text{ for each } f \in C^{\ell-1,1}. \tag{A3}$$

In the above, the constant $C$ may depend on $f$, but is independent of $e$ and $h$, and the integer $\ell \geq 1$ is called the order of convergence of the quadrature rule.

For convenience, we will often replace the element and node indices $e = 1, \ldots, E$ and $q = 1, \ldots, Q$ with a single, general index $a = 1, \ldots, n$, where $n = EQ$. We will use the multi- and single-index notation interchangeably with the understanding that there is a bijective map between the two.

5.2 Partition of unity functions

To each quadrature node $x_a$ in a decomposition of $\Gamma$ we associate nodal partition of unity functions $\zeta_a$ and $\widehat{\zeta}_a$. Specifically, we assume that these functions are continuous and take values in the interval $[0,1]$, and are complementary so that $\zeta_a(x) + \widehat{\zeta}_a(x) = 1$ for all $x \in \Gamma$. Moreover, we assume that $\zeta_a$ vanishes at least quadratically in a neighborhood of $x_a$, and that the support of $\widehat{\zeta}_a$ is bounded from above by a multiple of the mesh parameter $h$. Specifically, we assume

$$|\zeta_a(x)| \leq \frac{C|x - x_a|^2}{h^2}, \quad \text{diam}(\text{supp}(\widehat{\zeta}_a)) \leq Ch, \quad \forall a = 1, \ldots, n, \quad n \geq n_0. \tag{A4}$$

Appropriate functions $\zeta_a$ and $\widehat{\zeta}_a$ for each node $x_a$ can be constructed as follows. Consider an auxiliary decomposition of $\Gamma$ into Voronoi cells, where each cell contains a single quadrature point. Each cell can be mapped to a unit circle, with $x_a$ mapped to the center. A simple quadratic function $z = (x^2 + y^2)/2$ in the unit circle can be mapped back to the cell as the central part of $\zeta_a$. We can then introduce an offset boundary which is displaced outward from the cell boundary by a distance of $\varepsilon/2$, where $\varepsilon = \min_{a \neq b} |x_a - x_b|$. The mapped quadratic function, which by design has the value $1/2$ on the cell boundary, can be extended to achieve a value of $1$ on the offset boundary, and then further extended to the rest of $\Gamma$ with the constant value $1$ as illustrated in Figure 1. Notice that the functions $\zeta_a$ and $\widehat{\zeta}_a$ so constructed have the convenient nodal property that $\zeta_a(x_b) = 1 - \delta_{ab}$ and $\widehat{\zeta}_a(x_b) = \delta_{ab}$.

The nodal partition of unity functions $\zeta_a$ and $\widehat{\zeta}_a$ play an important role in the family of numerical methods that we introduce and in the associated convergence proofs. Specifically, these functions will help isolate the weak singularity of the double-layer kernel $H^\theta$ at each quadrature point and control the numerical error there. We remark that the construction outlined above leads to admissible partition of unity functions for the lowest-order method; admissible functions for higher-order methods would be different.
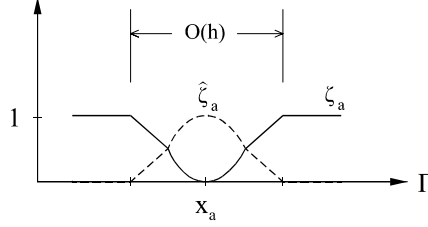
**Fig. 1** Illustration of the partition of unity functions $\zeta_a(x)$ and $\widehat{\zeta}_a(x)$ associated with a quadrature node $x_a$.

### 5.3 Discretization of integral equation

Let a decomposition, quadrature rule, and nodal partition of unity functions for $\Gamma$ be given. For any function $f$, let $\mathcal{G}_h^{\theta,\phi}$ and $\mathcal{H}_h^{\theta}$ denote approximations to $\mathcal{G}^{\theta,\phi}$ and $\mathcal{H}^{\theta}$ of the form

$$(\mathcal{G}_h^{\theta,\phi}f)(x) = \sum_{b=1}^{n} G_b^{\theta,\phi}(x)f(x_b), \quad (\mathcal{H}_h^{\theta}f)(x) = \sum_{b=1}^{n} H_b^{\theta}(x)f(x_b), \tag{41}$$

where $G_b^{\theta,\phi}$ and $H_b^{\theta}$ are functions to be specified. Moreover, in view of (36), let $\psi_h$ denote an approximation to $\psi$ defined by

$$\mathcal{G}_h^{\theta,\phi}\psi_h + \mathcal{H}_h^{\theta}\psi_h + c^{\theta}\psi_h = v. \tag{42}$$

The equation for $\psi_h$ can be reduced to an $n \times n$ linear system for the nodal values $\psi_h(x_a)$. Indeed, from (41) and (42) we get, for each $a = 1, \dots, n$,

$$\sum_{b=1}^{n} G_b^{\theta,\phi}(x_a)\psi_h(x_b) + \sum_{b=1}^{n} H_b^{\theta}(x_a)\psi_h(x_b) + c^{\theta}\psi_h(x_a) = v(x_a). \tag{43}$$

Notice that, for every solution of the discrete system (43), we obtain a solution of the continuous system (42), namely

$$\psi_h(x) = \frac{1}{c^{\theta}}\left[v(x) - \sum_{b=1}^{n} G_b^{\theta,\phi}(x)\psi_h(x_b) - \sum_{b=1}^{n} H_b^{\theta}(x)\psi_h(x_b)\right]. \tag{44}$$

Moreover, the converse is also true; every solution of the continuous system provides a solution of the discrete system by restriction to the nodes.

The method is completed by specifying the functions $G_b^{\theta,\phi}(x)$ and $H_b^{\theta}(x)$. In view of (37), (39) and (41)$_1$, we define $G_b^{\theta,\phi}(x) = G^{\theta,\phi}(x, x_b)W_b$. However, due to the weakly singular nature of the kernel function $H^{\theta}(x, y)$, a similar definition cannot be made for $H_b^{\theta}(x)$, because $H^{\theta}(x, x_b)$ is not continuous or even defined when $x = x_b$. Instead, for any integer $p \geq 0$ we define

$$H_b^{\theta}(x) = \zeta_b(x)H^{\theta}(x, x_b)W_b + \widehat{\zeta}_b(x)R_x^{\theta}(x_b), \tag{45}$$

where $R_x^{\theta}(x_b)$ is a local polynomial of degree $p$ at $x$, evaluated at quadrature point $x_b$. By a local polynomial at $x$ we mean a polynomial in any system of rectangular coordinates in the tangent plane with origin at $x$. For a Lyapunov surface $\Gamma$, such

polynomials are well-defined in an open neighborhood $O_x$ of each point $x$, and there is a uniform bound on the size of this neighborhood. The unknown coefficients in $R_x^\theta(x_b)$ are determined by enforcing the local moment conditions

$$(\mathcal{H}_h^\theta \eta_x f_x)(x) = (\mathcal{H}^\theta \eta_x f_x)(x), \text{ for all local polynomials } f_x \text{ up to degree } p. \quad (46)$$

Here $\eta_x$ is any given non-negative, cutoff function which is identically one in a fixed neighborhood of $x$, and which is identically zero outside of $O_x$. The above conditions lead to a linear system of equations for the unknown coefficients in $R_x^\theta(x_b)$, which can be solved for any given point $x$.

In this article, we consider only the lowest-order method with $p = 0$. In this case, the local polynomial $R_x^\theta$ reduces to a constant polynomial depending on $x$, the neighborhood $O_x$ can be taken as the entire surface $\Gamma$, and the cutoff function $\eta_x$ can be taken as unity. In view of (38) and $(41)_2$, the moment condition in (46) with constant $f_x$ yields

$$R_x^\theta = \frac{\int_\Gamma H^\theta(x,y)\, dA_y - \sum_{b'=1}^n \zeta_{b'}(x) H^\theta(x,x_{b'}) W_{b'}}{\sum_{b'=1}^n \widehat{\zeta}_{b'}(x)}. \quad (47)$$

Notice that $R_x^\theta$ is well-defined and bounded for any sequence of decompositions by properties of the nodal functions $\zeta_b$ and $\widehat{\zeta}_b$ and the kernel function $H^\theta$. The integral in the above expression can be evaluated exactly. Indeed, using the fact that constants are eigenfunctions of the Stokes double-layer potential [24,52,54,56], we have

$$\int_\Gamma H^\theta(x,y)\, dA_y = -c^\theta I, \quad \forall x \in \Gamma, \quad (48)$$

where $I$ is the identity matrix of the same dimension as $H^\theta$. The lowest-order method is thus defined by (41)–(45), with $R_x^\theta(x_b) \equiv R_x^\theta$ given by (47)–(48).

The nodal equations in (43) for the approximation $\psi_h$ can be put into a particularly simple form. Indeed, because our choice of the nodal partition of unity functions $\zeta_a$ and $\widehat{\zeta}_a$ has the property that $\zeta_a(x_b) = 1 - \delta_{ab}$ and $\widehat{\zeta}_a(x_b) = \delta_{ab}$, the equations become

$$\sum_{b=1}^n G^{\theta,\phi}(x_a,x_b)\psi_h(x_b)W_b + \sum_{\substack{b=1 \\ b \neq a}}^n H^\theta(x_a,x_b)[\psi_h(x_b) - \psi_h(x_a)]W_b = v(x_a). \quad (49)$$

Once the nodal values of $\psi_h$ are determined, they can be extended to a continuous function using the interpolation equation in (44). The discrete system above is similar to the classic singularity subtraction method discussed by various authors [8,37]. The factor $[\psi_h(x_b) - \psi_h(x_a)]$ can be interpreted as cancelling the weak singularity in $H^\theta(x_a,x_b)$. Indeed, since the sum extends over $b \neq a$ only, the product $H^\theta(x_a,x_b)[\psi_h(x_b) - \psi_h(x_a)]$ can be interpreted as vanishing when $b = a$. We remark that different choices of the partition of unity functions $\zeta_a$ and $\widehat{\zeta}_a$ could be made, which would lead to different nodal equations. However, the solvability and convergence results described below are independent of any specific choice.

The discrete system (49) can be written in a more standard form. Specifically, after collecting terms, we get

$$\sum_{b=1}^n A^{\theta,\phi}(x_a,x_b)\psi_h(x_b) = v(x_a), \quad \forall a = 1,\ldots,n, \quad (50)$$

where

$$A^{\theta,\phi}(x_a, x_b) = \begin{cases} G^{\theta,\phi}(x_a, x_b)W_b + H^\theta(x_a, x_b)W_b, & a \neq b \\ G^{\theta,\phi}(x_a, x_a)W_a - \displaystyle\sum_{\substack{c=1 \\ c \neq a}}^{n} H^\theta(x_a, x_c)W_c, & a = b. \end{cases} \quad (51)$$

This linear system is dense and non-symmetric, and can be solved using any suitable numerical technique.

5.4 Approximation of flow quantities

Various flow quantities of interest take the form of an integral of $\psi$ over $\Gamma$. For example, from (32), the resultant force and torque on $\Gamma$ about an arbitrary point $c$ are given by

$$F = -8\pi\theta \int_\gamma \psi(\varphi(\xi)) \, dA_\xi,$$
$$T = -8\pi\theta \int_\gamma (\xi - c) \times \psi(\varphi(\xi)) \, dA_\xi. \quad (52)$$

After a change of variable (see Section 4.1), these integrals can be transformed from the parallel surface $\gamma$ to the body surface $\Gamma$ to obtain

$$F = -8\pi\theta \int_\Gamma J^\phi(y)\psi(y) \, dA_y,$$
$$T = -8\pi\theta \int_\Gamma J^\phi(y)(\vartheta(y) - c) \times \psi(y) \, dA_y. \quad (53)$$

By discretizing these integrals using the same quadrature points and weights as before, we get the approximations

$$F_h = -8\pi\theta \sum_{b=1}^{n} J^\phi(x_b)\psi_h(x_b)W_b,$$
$$T_h = -8\pi\theta \sum_{b=1}^{n} J^\phi(x_b)(\vartheta(x_b) - c) \times \psi_h(x_b)W_b. \quad (54)$$

An approximation $Q_h$ to the volume flow rate $Q$ associated with $\Gamma$ can be obtained in a similar manner.

5.5 Solvability and convergence theorem

The following result establishes the solvability and convergence of the locally-corrected Nyström method defined in (41)–(45) and (47)–(48). We consider only the method with a local polynomial correction of degree $p = 0$, together with any quadrature rule of order $\ell \geq 1$.

**Theorem 2** *Under conditions* (A1)–(A4), *there exists a unique approximation* $\psi_h \in C^0$ *for any closed, bounded Lyapunov surface* $\Gamma \in C^{1,1}$, *parallel offset parameter* $\phi \in (0, \phi_\Gamma)$, *interpolation parameter* $\theta \in (0, 1)$ *and boundary data* $v \in C^0$ *for all* $h > 0$ *sufficiently small. Moreover, if* $\psi \in C^{m,1}$ *and* $\Gamma \in C^{m+1,1}$, *then as* $h \to 0$

$$||\psi_h - \psi||_\infty \to 0, \qquad \forall \ell \geq 1, m \geq 0,$$

$$||\psi_h - \psi||_\infty \leq Ch, \quad \forall \ell \geq 1, m \geq 1.$$

Thus, under suitable assumptions, the method defined by (41)–(45) and (47)–(48) is convergent in the usual maximum or $C^0$-norm. The rate of convergence depends on the regularity index $m$ of the exact solution $\psi$ and the surface $\Gamma$. In the minimal regularity case with $m = 0$, there is no lower bound on the rate, and in the higher regularity case with $m \geq 1$, the rate is at least linear. The linear rate is independent of the order $\ell \geq 1$ of the quadrature rule due to the low degree $p = 0$ of the polynomial correction. Indeed, higher rates of convergence could be obtained with higher degrees of correction. Notice that the linear rate of convergence is a lower bound; it could possibly be higher in certain circumstances, for example in smooth problems with periodicity, for which some quadrature rules are known to have special properties [15, 39]. We remark that the method considered here is based on open quadrature rules as required by condition (A2). The entire family of methods with arbitrary degree of correction $p \geq 0$ for a general class of boundary integral equations is studied in a separate work [28].

Notice that a discrete version of the above theorem in terms of purely nodal quantities defined via the system in (50) also holds. Specifically, the theorem establishes the convergence of the nodal error $\max_b |\psi_h(x_b) - \psi(x_b)|$ without the explicit need for the Nyström interpolation formula in (44) and the nodal partition of unity functions. Moreover, the conditions of the theorem are met by the simplest of quadrature rules; for example, one-point rules of the barycentric type for triangular or quadrilateral elements on their standard domains would be sufficient. As a result, the theorem establishes the convergence of a method similar to the classic singularity subtraction method as considered previously by various authors [8, 37]. The two methods lead to apparently identical discrete systems for the nodal approximations, but differ in how the nodal approximations are interpolated over the surface. Convergence results for this method appear to be not well-known. The proof of the results outlined here makes crucial use of the structure of the nodal functions $H_b^\theta(x)$ defined in (45), the moment conditions defined in (46), and various properties of the nodal partition of unity functions $\zeta_b$ and $\widehat{\zeta_b}$. Such ingredients appear to have not been considered in previous studies of the classic method.

The proof of the theorem consists of three main steps and is based on the theory of collectively compact operators [7], which plays a fundamental role in the analysis of Nyström methods [10, 36]. Specifically, on the space $C^0$, we consider the operator $\mathcal{A}^{\theta,\phi}$ and the family of operators $\mathcal{A}_h^{\theta,\phi}$ defined as

$$\mathcal{A}^{\theta,\phi} = \mathcal{G}^{\theta,\phi} + \mathcal{H}^\theta, \quad \mathcal{A}_h^{\theta,\phi} = \mathcal{G}_h^{\theta,\phi} + \mathcal{H}_h^\theta. \tag{55}$$

The first step in the proof is to establish the uniform continuity and uniform convergence of $\mathcal{A}_h^{\theta,\phi} f$ on $\Gamma$ for each $f$, and thereby establish the collective compactness of the family $\mathcal{A}_h^{\theta,\phi}$. The second step is to bound the approximation errors between

$\mathcal{A}_h^{\theta,\phi} f$ and $\mathcal{A}^{\theta,\phi} f$ on $\Gamma$ under different regularity assumptions on $f$. In the third step, a fundamental estimate for collectively compact operators then allows us to bound the error between $\psi_h$ and $\psi$ by the error between $\mathcal{A}_h^{\theta,\phi}\psi$ and $\mathcal{A}^{\theta,\phi}\psi$. The detailed proof of the theorem is presented in a separate work [28] and relies on a Tricomi-like property of the Stokes double-layer potential. A proof under different regularity assumptions and conditions can be found in [43, Theorem 7.4.3].

Another implication of the above theorem is that the approximate flow quantities $F_h$, $T_h$ and $Q_h$ converge to their exact values $F$, $T$ and $Q$ at the same rate as $\psi_h$ converges to $\psi$. This follows from the fact that $F$, $T$ and $Q$ are bounded linear functionals on the space $C^0$ and that $\psi_h$ converges to $\psi$ in $C^0$. Just as before, in the minimal regularity case with $m = 0$, there is no lower bound on the rate of convergence of $F_h$, $T_h$ and $Q_h$, and in the higher regularity case with $m \geq 1$, the rate is at least linear. Moreover, the rate could possibly be higher than linear in certain circumstances as discussed above.

## 6 Numerical experiments

Here we illustrate the convergence and conditioning of the lowest-order, locally-corrected Nyström method introduced above. We present results for four different body geometries of varying symmetry, genus, curvature and regularity: an ellipsoid, torus, straight tube and helical tube. In the latter two cases the tube ends were closed with hemi-spherical endcaps. For each body, we computed the maximum and minimum singular values of the coefficient matrix in (50) and examined its condition number, in the standard Euclidean norm, as a function of the parameters $\theta$ and $\phi$. For one or more prescribed motions of each body, we also computed the resultant force and torque about the origin of a body-fixed frame, and examined various measures of convergence for different values of $\theta$ and $\phi$.

### 6.1 Methods

In accordance with the Nyström scheme, we decomposed the surface of each body into non-overlapping patches, each of which was parameterized over a planar, rectangular domain. We then subdivided each patch into quadrilateral elements, and in each element we used a $d \times d$ tensor product Gauss-Legendre quadrature rule, where $d = 1$ or $2$, with order of convergence $\ell = 2d$. For the ellipsoid we employed six patches based on stereographic projection from the faces of a bounding cube. For the torus we employed a single patch based on an explicit parameterization of the axial curve. For the straight and helical tubes we employed multiple patches based on explicit parameterizations of the axial curve and endcaps.

Singular values, and consequently the condition number, of the coefficient matrix in (50) were computed using standard matrix routines for the singular value decomposition. The resultant force $F$ and torque $T$ on each body were approximated by solving the linear algebraic system (50) of size $(3EQ) \times (3EQ)$, where $E$ is the total number of elements and $Q = d^2$ is the number of quadrature points per element. Because this system was non-symmetric and well-conditioned, we used a GMRES iterative solver with no pre-conditioning and a residual tolerance of $10^{-8}$ as implemented in Matlab. Using the solution of (50), we computed the

approximations $F_h$ and $T_h$ according to (54). The total number $E$ of elements for each surface was varied up to a maximum value of approximately 3250, and the number $Q$ of quadrature points per element was either 1 or 4, hence the total number $3EQ$ of unknowns in the linear system was varied up to a maximum value of approximately 39000.

6.2 Results

*Ellipsoid example.* Figure 2 shows conditioning results as a function of $\theta$ and $\phi$ for an ellipsoid. The ellipsoid was centered at the origin and defined by the equation $x^2/a^2 + y^2/b^2 + z^2/c^2 = 1$ with $(a, b, c) = (1, 0.8, 0.6)$. Results are given for the $1 \times 1$ Gauss rule and two different meshes. The fineness of a mesh is quantified by the element size parameter $h$, which is proportional to the maximum element size, and also the average element size because of the quasi-uniform nature of the mesh. Results for the $2 \times 2$ rule were nearly identical and are omitted for brevity.

Plot (a) of Figure 2 illustrates the geometry of the ellipsoid. The ellipsoid parameters were chosen so as to produce a surface with moderate, non-constant curvature. When $a \geq b \geq c > 0$, the maximum curvature is $\kappa_\Gamma = a/c^2$, which gives a maximum offset distance of $\phi_\Gamma = c^2/a$ for the parallel surface. Plot (b) shows the singular values $\sigma_{\min} \geq 0$ and $\sigma_{\max} \geq 0$ as a function of $\theta \in (0, 1)$ for different values of $\phi/\phi_\Gamma \in (0, 1)$ for two different meshes. The results for the two meshes are indistinguishable and suggest that the singular values converge rather quickly with respect to the element size $h$. In agreement with the results outlined in Section 4.2, $\sigma_{\min}$ is non-zero and vanishes only when $\theta \to 0$ and $\theta \to 1$. For each fixed $\phi$, we observe that $\sigma_{\min}$ has a single local maximum and no local minimum with respect to $\theta$, whereas $\sigma_{\max}$ has a single local minimum and no local maximum. For each fixed $\theta$, we observe that $\sigma_{\min}$ and $\sigma_{\max}$ both increase as $\phi$ decreases.

Plot (c) shows the condition number $\sigma_{\max}/\sigma_{\min}$ as a function of $\theta \in (0, 1)$ for different values of $\phi/\phi_\Gamma \in (0, 1)$ for two different meshes. Because the condition number becomes unbounded as $\theta \to 0$ and $\theta \to 1$, we consider only a restricted domain away from these limits for clarity. As in plot (b), the results for the two meshes are indistinguishable. For each fixed $\phi$, we observe that the condition number has a single local minimum and no local maximum with respect to $\theta$. For each fixed $\theta$, we observe that the condition number decreases as $\phi$ decreases, except near the right boundary of the $\theta$-domain. In agreement with the expectations discussed in Section 4.2, optimal conditioning occurs near $\theta = 1/2$ for small $\phi > 0$. Notice that, in the limit case $\phi = 0$, the single-layer operator in our formulation becomes weakly singular, which would require special treatment. The plots show that any choice of parameters with $\theta \in [1/3, 2/3]$ and $\phi/\phi_\Gamma \in [1/8, 1/2]$ would yield an extremely well-conditioned linear system with a relatively mesh-independent condition number $\sigma_{\max}/\sigma_{\min} \leq 10^{1.1}$.

Figure 3 shows convergence results for the resultant force and torque about the origin on the ellipsoid obtained with the $1 \times 1$ and $2 \times 2$ quadrature rules. Results are given for two different parameter pairs: $(\theta, \phi/\phi_\Gamma) = (1/2, 1/4)$ and $(1/2, 1/2)$. Moreover, results are given for two independent boundary conditions: translation along the $x$-axis with unit velocity, and rotation about the same axis with unit angular velocity. By symmetry, the force and torque have the form $F = (F_x, 0, 0)$
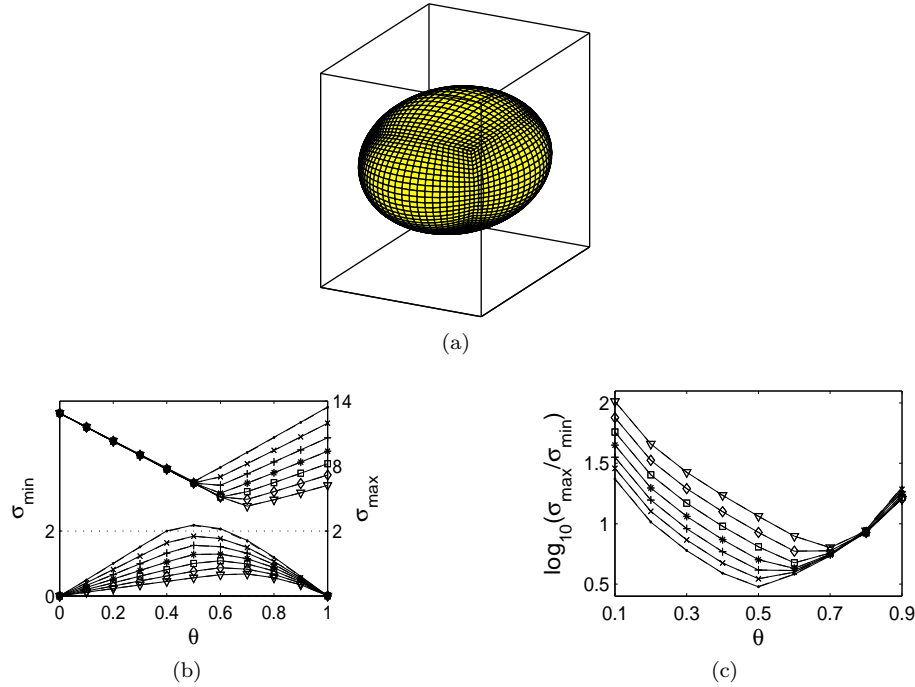
(a)



(b)                                                    (c)

**Fig. 2** Conditioning of Nyström system with $1 \times 1$ Gauss quadrature rule for an ellipsoid. (a): Illustration of geometry. (b): Plot of singular values $\sigma_{\min}$ and $\sigma_{\max}$ versus $\theta$ for fixed values of $\phi$. The dotted horizontal line provides a reference for the two vertical scales. (c): Plot of log of condition number $\sigma_{\max}/\sigma_{\min}$ versus $\theta$ for fixed values of $\phi$. Dots, crosses, pluses, stars, squares, diamonds and triangles denote results for $\phi/\phi_\Gamma = 1/8, 2/8, \ldots, 7/8$. Solid and dashed lines (completely overlapped) denote results for $h = 0.10, 0.07$.

and $T = (0, 0, 0)$ for the translational motion, and $F = (0, 0, 0)$ and $T = (T_x, 0, 0)$ for the rotational motion.

Plots (a) and (b) of Figure 3 show convergence results for the magnitudes of $F_h$ and $T_h$ in the translational and rotational motions, respectively, as a function of the element size parameter $h$. In all computations the appropriate entries in both $F_h$ and $T_h$ were found to be zero within machine precision for each type of motion. Thus the errors illustrated can be attributed to the appropriate non-zero components. The data reveals that different values of the parameter pair $(\theta, \phi/\phi_\Gamma)$ can lead to different convergence characteristics. For the parameter pair $(1/2, 1/4)$, the magnitudes of $F_h$ and $T_h$ approach their asymptotic values monotonically as $h$ decreases for the range of meshes considered. In contrast, for the parameter pair $(1/2, 1/2)$, the magnitudes of $F_h$ and $T_h$ approach their asymptotic values in a non-monotonic manner. This behavior is illustrated in plot (c), which is a magnified view of the data in plot (b).

Plots (d) and (e) of Figure 3 show the differences in the computed values of $F_h$ and $T_h$ between successive meshes as a function of $h$ for each of the two motions. The different convergence characteristics corresponding to the different values of $(\theta, \phi/\phi_\Gamma)$ is evident. For the parameter pair $(1/2, 1/4)$, the solution differences de-
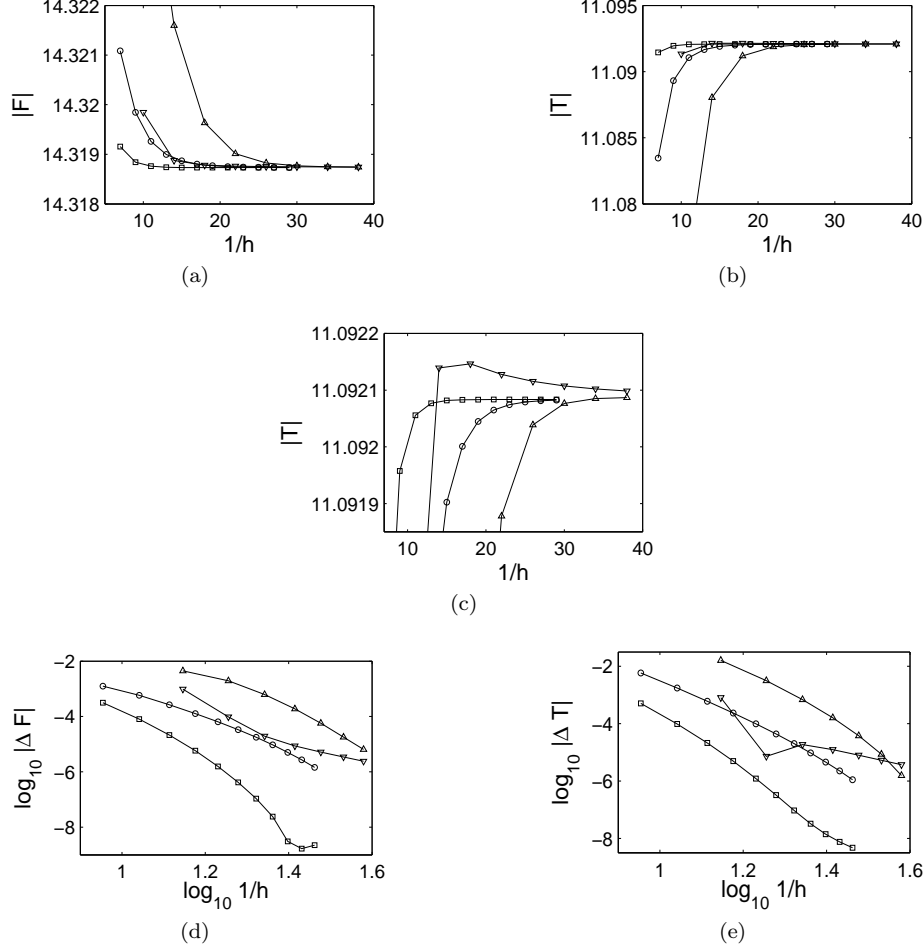
**Fig. 3** Convergence results for resultant force $F$ and torque $T$ on an ellipsoid. Computations were performed with a sequence of meshes with element sizes $h_k$. (a),(b): Plots of $|F_{h_k}|$ and $|T_{h_k}|$ versus $1/h_k$ for the translational and rotational motion, respectively. (c): Magnified view of (b). (d),(e): Plots of $\log_{10}|F_{h_k} - F_{h_{k-1}}|$ and $\log_{10}|T_{h_k} - T_{h_{k-1}}|$ versus $\log_{10}(1/h_k)$ for the translational and rotational motion, respectively. Upward-pointing triangles and circles denote results for the $1 \times 1$ and $2 \times 2$ rules with $(\theta, \phi/\phi_\Gamma) = (1/2, 1/4)$. Downward-pointing triangles and squares denote results for the $1 \times 1$ and $2 \times 2$ rules with $(\theta, \phi/\phi_\Gamma) = (1/2, 1/2)$.

crease monotonically as the mesh is refined, whereas for the pair $(1/2, 1/2)$, the solution differences behave non-monotonically. This behavior is a simple consequence of the monotonicity or non-monotonicity of the corresponding curves in plots (a) and (b). In particular, local extrema in the curves in (a) and (b) cause local extrema in the curves in (d) and (e), which become magnified by virtue of the log scale. For the force data in plot (d), non-monotonicity becomes apparent only on rather refined meshes (where the GMRES tolerance becomes an issue), whereas for the torque data in plot (e), it becomes apparent on modest meshes.
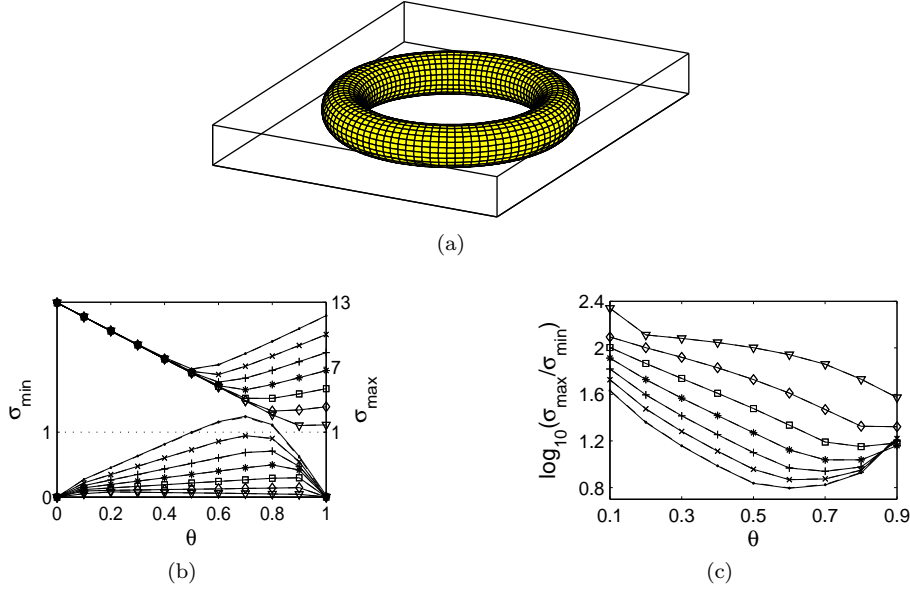
(a)



(b)



(c)

**Fig. 4** Conditioning of Nyström system with $1 \times 1$ Gauss quadrature rule for a torus. (a): Illustration of geometry. (b): Plot of singular values $\sigma_{\min}$ and $\sigma_{\max}$ versus $\theta$ for fixed values of $\phi$. The dotted horizontal line provides a reference for the two vertical scales. (c): Plot of log of condition number $\sigma_{\max}/\sigma_{\min}$ versus $\theta$ for fixed values of $\phi$. Dots, crosses, pluses, stars, squares, diamonds and triangles denote results for $\phi/\phi_\Gamma = 1/8, 2/8, \ldots, 7/8$. Solid and dashed lines (completely overlapped) denote results for $h = 0.03, 0.02$.

For any sequence $h_k \to 0$ of decreasing mesh sizes, our convergence result in Theorem 2 implies that $|F_{h_k} - F| \to 0$ and $|T_{h_k} - T| \to 0$, where the convergence rate is at least linear due to the regular nature of the geometry and data. Because the exact values $F$ and $T$ are not known, we instead can examine the errors $|F_{h_k} - F_{h_{k-1}}|$ and $|T_{h_k} - T_{h_{k-1}}|$, whose convergence rate must also be at least linear by the triangle inequality. The behavior of these errors is illustrated in plots (d) and (e). Due to the non-linear nature of the curves in these plots it is difficult to assign meaningful convergence rates. Nevertheless, in the non-linear but monotonic case corresponding to the parameter pair $(1/2, 1/4)$, the observed rates were significantly higher than linear or first-order: the observed rates were between eighth- and twelfth-order. Interestingly, the observed rates for the $1 \times 1$ rule were as high or higher than those for the $2 \times 2$ rule in this case. Although the convergence curves for $(1/2, 1/4)$ are better behaved than those for $(1/2, 1/2)$, the numerical accuracies achieved with the second pair are, for the most part, higher than those achieved with the first. For the $2 \times 2$ rule with the pair $(1/2, 1/4)$, the relative changes in $F_h$ and $T_h$ between the finest two meshes were each of order $10^{-7}$. For the same quadrature rule and the pair $(1/2, 1/2)$, the relative changes in $F_h$ and $T_h$ were each of order $10^{-9}$.

*Torus example.* Figure 4 shows conditioning results as a function of $\theta$ and $\phi$ for a torus, which in contrast to the previous example has a different genus and principal curvatures of varying sign. The axial curve of the torus was a circle of
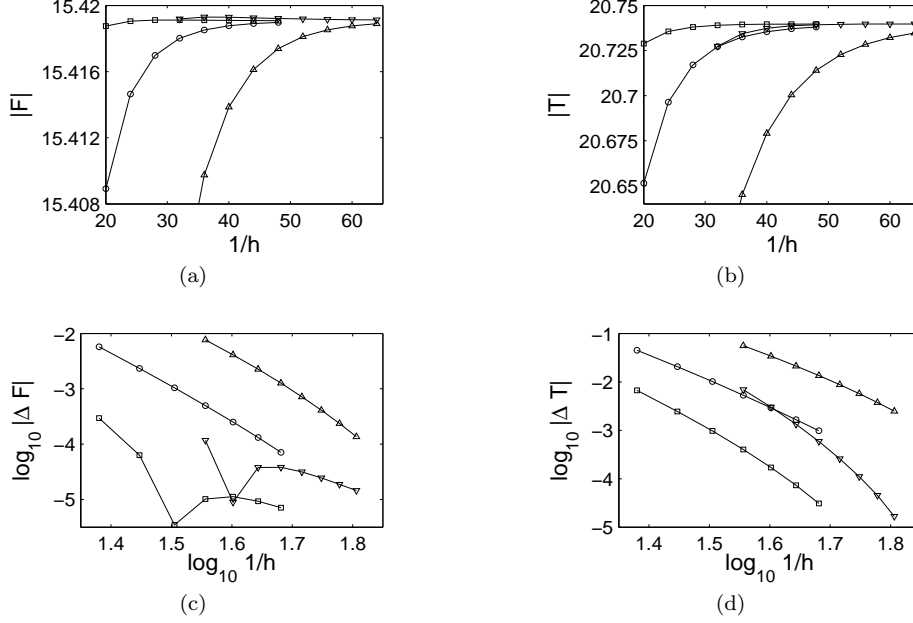
**Fig. 5** Convergence results for resultant force $F$ and torque $T$ on a torus. Computations were performed with a sequence of meshes with element sizes $h_k$. (a),(b): Plots of $|F_{h_k}|$ and $|T_{h_k}|$ versus $1/h_k$ for the translational and rotational motion, respectively. (c),(d): Plots of $\log_{10}|F_{h_k} - F_{h_{k-1}}|$ and $\log_{10}|T_{h_k} - T_{h_{k-1}}|$ versus $\log_{10}(1/h_k)$ for the translational and rotational motion, respectively. Upward-pointing triangles and circles denote results for the $1 \times 1$ and $2 \times 2$ rules with $(\theta, \phi/\phi_\Gamma) = (1/2, 1/4)$. Downward-pointing triangles and squares denote results for the $1 \times 1$ and $2 \times 2$ rules with $(\theta, \phi/\phi_\Gamma) = (1/2, 1/2)$.

radius $\rho = 1$ centered at the origin in the $xy$-plane, and the tube section was a circle of radius $r = 0.2$. Results are given for the $1 \times 1$ Gauss rule and two different meshes. As for the ellipsoid, results for the $2 \times 2$ rule were nearly identical and are omitted for brevity. Plot (a) illustrates the geometry. The torus parameters were chosen so as to produce a slender tubular surface with rather high curvature. For this surface the maximum curvature is $\kappa_\Gamma = 1/r$, which gives a maximum offset distance of $\phi_\Gamma = r$. Plots (b) and (c) are analogous to the ellipsoid example. As before, the results for the two meshes are indistinguishable. In agreement with the results outlined in Section 4.2, $\sigma_{\min}$ is non-zero and vanishes when $\theta \to 0$ and $\theta \to 1$. Moreover, in contrast to the case with the ellipsoid, $\sigma_{\min}$ also vanishes in the limit $\phi/\phi_\Gamma \to 1$ because the parallel surface degenerates to zero area in this case. The behavior of the singular values and the condition number is similar to that observed before. As with the ellipsoid, optimal conditioning occurs near $\theta = 1/2$ for small $\phi > 0$, although here slightly larger values of $\theta$ are favored. Any choice of parameters with $\theta \in [1/3, 2/3]$ and $\phi/\phi_\Gamma \in [1/8, 1/2]$ would yield an extremely well-conditioned linear system with a relatively mesh-independent condition number $\sigma_{\max}/\sigma_{\min} \leq 10^{1.6}$.

Figure 5 shows convergence results for the resultant force and torque about the origin on the torus obtained with the $1 \times 1$ and $2 \times 2$ quadrature rules. Results
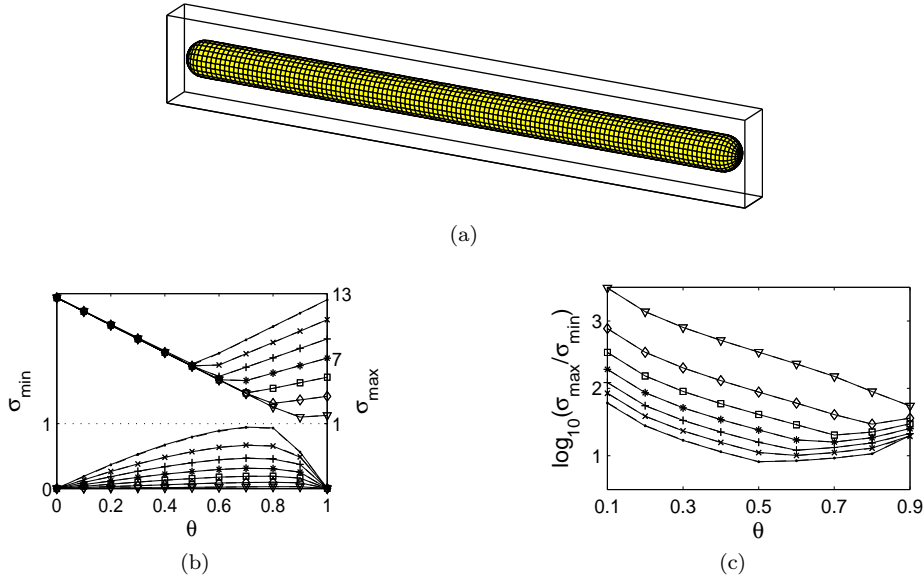
(a)



(b)



(c)

**Fig. 6** Conditioning of Nyström system with $1 \times 1$ Gauss quadrature rule for a straight tube. (a): Illustration of geometry. (b): Plot of singular values $\sigma_{\min}$ and $\sigma_{\max}$ versus $\theta$ for fixed values of $\phi$. The dotted horizontal line provides a reference for the two vertical scales. (c): Plot of log of condition number $\sigma_{\max}/\sigma_{\min}$ versus $\theta$ for fixed values of $\phi$. Dots, crosses, pluses, stars, squares, diamonds and triangles denote results for $\phi/\phi_\Gamma = 1/8, 2/8, \ldots, 7/8$. Solid and dashed lines (completely overlapped) denote results for $h = 0.14, 0.11$.

are given for two different parameter pairs: $(\theta, \phi/\phi_\Gamma) = (1/2, 1/4)$ and $(1/2, 1/2)$. Moreover, results are given for two independent boundary conditions: translation along the $x$-axis with unit velocity, and rotation about the same axis with unit angular velocity. As before, by symmetry, the force and torque have the form $F = (F_x, 0, 0)$ and $T = (0, 0, 0)$ for the translational motion, and $F = (0, 0, 0)$ and $T = (T_x, 0, 0)$ for the rotational motion. Plots (a) through (d) of Figure 5 are analogous to the ellipsoid example. In our computations, we again found that the appropriate entries in both $F_h$ and $T_h$ were zero within machine precision for each type of motion. Moreover, for the range of meshes considered, we found that the two values of the pair $(\theta, \phi/\phi_\Gamma)$ produced convergence characteristics similar to those observed before: monotonic convergence for $(1/2, 1/4)$, and non-monotonic convergence for $(1/2, 1/2)$. The non-monotonicity for this latter case is apparent in the force data in plot (c). In the monotonic case corresponding to $(1/2, 1/4)$, the observed rates for solution differences were significantly higher than first-order: the observed rates were approximately sixth-order. As before, the numerical accuracies achieved with $(1/2, 1/2)$ are higher than those achieved with $(1/2, 1/4)$. For the $2 \times 2$ rule with the pair $(1/2, 1/4)$, the relative changes in $F_h$ and $T_h$ between the finest two meshes were of order $10^{-5}$ and $10^{-4}$, respectively. For the same quadrature rule and the pair $(1/2, 1/2)$, the relative changes in $F_h$ and $T_h$ were of order $10^{-6}$ and $10^{-5}$, respectively.
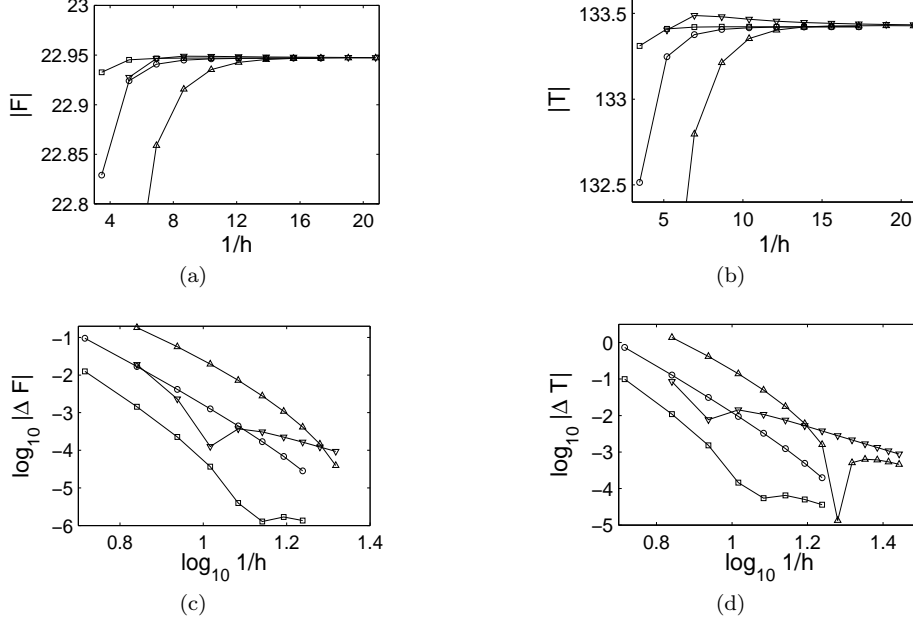
**Fig. 7** Convergence results for resultant force $F$ and torque $T$ on a straight tube. Computations were performed with a sequence of meshes with element sizes $h_k$. (a),(b): Plots of $|F_{h_k}|$ and $|T_{h_k}|$ versus $1/h_k$ for the translational and rotational motion, respectively. (c),(d): Plots of $\log_{10}|F_{h_k} - F_{h_{k-1}}|$ and $\log_{10}|T_{h_k} - T_{h_{k-1}}|$ versus $\log_{10}(1/h_k)$ for the translational and rotational motion, respectively. Upward-pointing triangles and circles denote results for the $1 \times 1$ and $2 \times 2$ rules with $(\theta, \phi/\phi_\Gamma) = (1/2, 1/4)$. Downward-pointing triangles and squares denote results for the $1 \times 1$ and $2 \times 2$ rules with $(\theta, \phi/\phi_\Gamma) = (1/2, 1/2)$.

*Straight tube example.* Figure 6 shows conditioning results as a function of $\theta$ and $\phi$ for a straight tube, which in contrast to the previous examples is non-smooth but in the $C^{1,1}$ regularity class due to jumps in curvature. The axial curve of the tube was a line segment along the $z$-axis of length $\ell = 2\pi$ centered at the origin. The tube had uniform, circular cross-sections of radius $r = 0.2$, and hemispherical endcaps of the same radius. Results are given for the $1 \times 1$ Gauss rule and two different meshes. As before, results for the $2 \times 2$ rule were nearly identical and are omitted for brevity. Plot (a) illustrates the geometry. For this surface the maximum curvature is $\kappa_\Gamma = 1/r$, which gives a maximum offset distance of $\phi_\Gamma = r$. Plots (b) and (c) are analogous to the previous examples. As before, the results for the two meshes are indistinguishable. In agreement with the results outlined in Section 4.2, $\sigma_{\min}$ is non-zero and vanishes when $\theta \to 0$, $\theta \to 1$ and $\phi/\phi_\Gamma \to 1$. The behavior of the singular values and the condition number is similar to that observed before. Optimal conditioning again occurs near $\theta = 1/2$ for small $\phi > 0$. Any choice of parameters with $\theta \in [1/3, 2/3]$ and $\phi/\phi_\Gamma \in [1/8, 1/2]$ would yield an extremely well-conditioned linear system with a relatively mesh-independent condition number $\sigma_{\max}/\sigma_{\min} \leq 10^{1.8}$.

Figure 7 shows convergence results for the resultant force and torque about the origin on the straight tube obtained with the $1 \times 1$ and $2 \times 2$ quadrature rules.
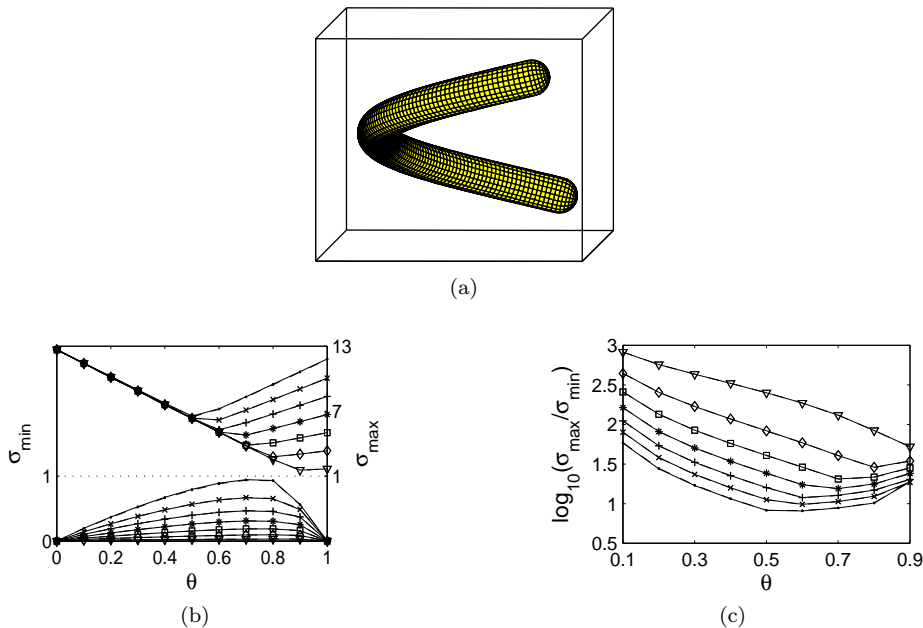
(a)



(b)



(c)

**Fig. 8** Conditioning of Nyström system with $1 \times 1$ Gauss quadrature rule for a helical tube. (a): Illustration of geometry. (b): Plot of singular values $\sigma_{\min}$ and $\sigma_{\max}$ versus $\theta$ for fixed values of $\phi$. The dotted horizontal line provides a reference for the two vertical scales. (c): Plot of log of condition number $\sigma_{\max}/\sigma_{\min}$ versus $\theta$ for fixed values of $\phi$. Dots, crosses, pluses, stars, squares, diamonds and triangles denote results for $\phi/\phi_\Gamma = 1/8, 2/8, \ldots, 7/8$. Solid and dashed lines (completely overlapped) denote results for $h = 0.14, 0.11$.

Results are given for two different parameter pairs: $(\theta, \phi/\phi_\Gamma) = (1/2, 1/4)$ and $(1/2, 1/2)$. Moreover, results are given for two independent boundary conditions: translation along the $x$-axis with unit velocity, and rotation about the same axis with unit angular velocity. Again, by symmetry, the force and torque have the form $F = (F_x, 0, 0)$ and $T = (0, 0, 0)$ for the translational motion, and $F = (0, 0, 0)$ and $T = (T_x, 0, 0)$ for the rotational motion. Plots (a) through (d) of Figure 7 are analogous to the previous examples. We again found that the appropriate entries in both $F_h$ and $T_h$ were zero within machine precision for each type of motion. In contrast to before, we found that each of the two values of the pair $(\theta, \phi/\phi_\Gamma)$ produced non-monotonic convergence characteristics for the range of meshes considered. The non-monotonicity is apparent in the data in plots (c) and (d). As before, the numerical accuracies achieved with $(1/2, 1/2)$ are, for the most part, higher than those achieved with $(1/2, 1/4)$. For the $2 \times 2$ rule with the pair $(1/2, 1/4)$, the relative changes in $F_h$ and $T_h$ between the finest two meshes were each of order $10^{-5}$. For the same quadrature rule and the pair $(1/2, 1/2)$, the relative changes in $F_h$ and $T_h$ were of order $10^{-7}$ and $10^{-6}$, respectively.

*Helical tube example.* Figure 8 shows conditioning results as a function of $\theta$ and $\phi$ for a helical tube, which is non-smooth but in the $C^{1,1}$ regularity class due to jumps in curvature and is less symmetric than the previous examples. The axial curve of the tube was a helical curve about the $z$-axis with radius $\rho = 2$, pitch
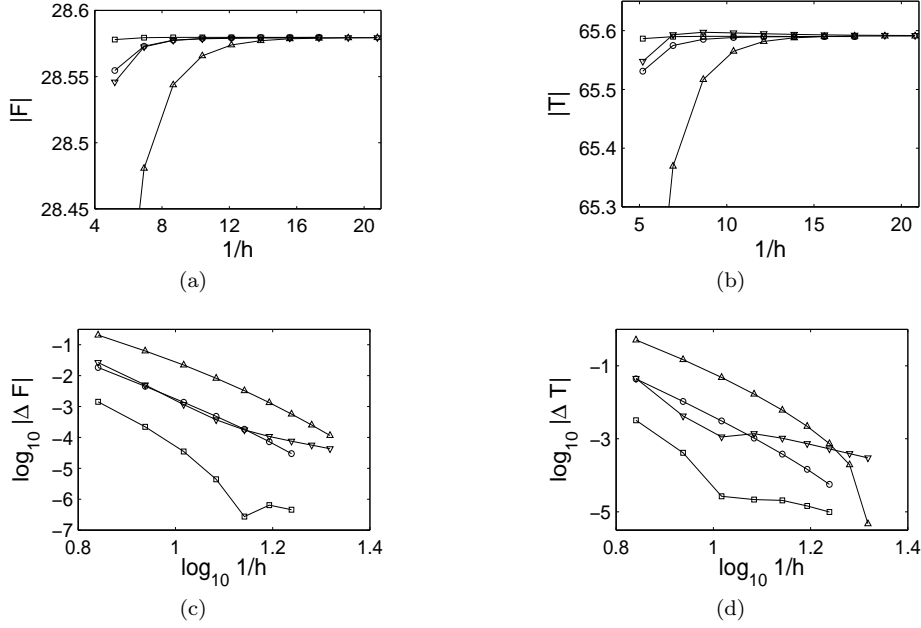
**Fig. 9** Convergence results for resultant force $F$ and torque $T$ on a helical tube. Computations were performed with a sequence of meshes with element sizes $h_k$. (a),(b): Plots of $|F_{h_k}|$ and $|T_{h_k}|$ versus $1/h_k$. (c),(d): Plots of $\log_{10} |F_{h_k} - F_{h_{k-1}}|$ and $\log_{10} |T_{h_k} - T_{h_{k-1}}|$ versus $\log_{10}(1/h_k)$. Upward-pointing triangles and circles denote results for the $1 \times 1$ and $2 \times 2$ rules with $(\theta, \phi/\phi_\Gamma) = (1/2, 1/4)$. Downward-pointing triangles and squares denote results for the $1 \times 1$ and $2 \times 2$ rules with $(\theta, \phi/\phi_\Gamma) = (1/2, 1/2)$.

$\lambda = 3$, and arclength $\ell = 2\pi$. The tube had uniform, circular cross-sections of radius $r = 0.2$, and hemi-spherical endcaps of the same radius. Results are given for the $1 \times 1$ Gauss rule and two different meshes. Again, results for the $2 \times 2$ rule were nearly identical and are omitted for brevity. Plot (a) illustrates the geometry. For this surface the maximum curvature is $\kappa_\Gamma = 1/r$, which gives a maximum offset distance of $\phi_\Gamma = r$. Plots (b) and (c) are analogous to the previous examples. As before, the results for the two meshes are indistinguishable. In agreement with the results outlined in Section 4.2, $\sigma_{\min}$ is non-zero and vanishes when $\theta \to 0$, $\theta \to 1$ and $\phi/\phi_\Gamma \to 1$. The behavior of the singular values and the condition number is similar to that observed previously. Optimal conditioning again occurs near $\theta = 1/2$ for small $\phi > 0$. Any choice of parameters with $\theta \in [1/3, 2/3]$ and $\phi/\phi_\Gamma \in [1/8, 1/2]$ would yield an extremely well-conditioned linear system with a relatively mesh-independent condition number $\sigma_{\max}/\sigma_{\min} \leq 10^{1.8}$.

Figure 9 shows convergence results for the resultant force and torque about the origin on the helical tube obtained with the $1 \times 1$ and $2 \times 2$ quadrature rules. Results are given for two different parameter pairs: $(\theta, \phi/\phi_\Gamma) = (1/2, 1/4)$ and $(1/2, 1/2)$. In contrast to the previous examples, results are given for a single boundary condition: rotation about the $x$-axis with unit angular velocity. In this case, the resultant force and torque are not known to have any special form. Plots

| Parameters | | Ellipsoid | | Torus | | Straight Tube | | Helical Tube | |
|---|---|---|---|---|---|---|---|---|---|
| | | $h_{max}$ | $h_{min}$ | $h_{max}$ | $h_{min}$ | $h_{max}$ | $h_{min}$ | $h_{max}$ | $h_{min}$ |
| $\theta = \frac{1}{2}$ | $1 \times 1$ | 9 | 9 | 8 | 8 | 14 | 15 | 25 | 26 |
| $\phi/\phi_\Gamma = \frac{1}{4}$ | $2 \times 2$ | 9 | 9 | 9 | 9 | 15 | 15 | 25 | 25 |
| $\theta = \frac{1}{2}$ | $1 \times 1$ | 9 | 9 | 8 | 8 | 17 | 17 | 37 | 37 |
| $\phi/\phi_\Gamma = \frac{1}{2}$ | $2 \times 2$ | 9 | 9 | 10 | 10 | 17 | 17 | 37 | 37 |

**Table 1** Number of GMRES iterations with relative error $10^{-8}$

(a) through (d) of Figure 9 are analogous to the previous examples, with the exception that only one type of motion is considered. For this single motion the force and torque were each found to possess three non-zero components in contrast to before. As in the case of the straight tube, we found that each of the two values of the pair $(\theta, \phi/\phi_\Gamma)$ produced non-monotonic convergence characteristics for the range of meshes considered. The non-monotonicity is apparent in the data in plots (c) and (d). As before, the numerical accuracies achieved with $(1/2, 1/2)$ are, for the most part, higher than those achieved with $(1/2, 1/4)$. For the $2 \times 2$ rule with the pair $(1/2, 1/4)$, the relative changes in $F_h$ and $T_h$ between the finest two meshes were each of order $10^{-5}$. For the same quadrature rule and the pair $(1/2, 1/2)$, the relative changes in $F_h$ and $T_h$ were of order $10^{-7}$ and $10^{-6}$, respectively.

*Linear solve characteristics.* Table 1 shows the number of GMRES iterations, without pre-conditioning, required to solve the linear algebraic system (50) for all our examples. Results are given for the coarsest and finest meshes for each geometry as indicated by the element size parameters $h_{\max}$ and $h_{\min}$. In agreement with the conditioning results outlined above, the number of iterations is relatively small for each of the parameter pairs $(\theta, \phi/\phi_\Gamma)$ and geometries considered, and is relatively independent of the mesh and quadrature rule. The data reveals a slight dependence of the iteration count on the pair $(\theta, \phi/\phi_\Gamma)$ and a moderate dependence on the geometry. This dependence is consistent with our observations that the pair $(1/2, 1/4)$ generally leads to a better conditioned system than $(1/2, 1/2)$, and that the condition numbers for the ellipsoid and torus were lower than those for the straight and helical tubes.

**References**

1. S.A. Allison and V.T. Tran, Modeling the electrophoresis of rigid polyions: Application to lysozyme, *Biophys. J.* **68**, (1995) 2261–2270.
2. S.A. Allison and S. Mazur, Modeling the free solution electrophoretic mobility of short DNA fragments, *Biopolymers* **46** (1998) 359–373.
3. S.A. Allison and C. Chen and D. Stigter, The length dependence of the translational diffusion, free solution electrophoretic mobility, and electrophoretic tether force of rigid rod-like model duplex DNA, *Biophys. J.* **81** (2001) 2558–2568.
4. S. Aragon, A precise boundary element method for macromolecular transport properties, *J. Comp. Chem.* **25** (2004) 1191–1205.
5. S. Aragon and D.K. Hahn, Precise boundary element computation of protein transport properties: diffusion tensors, specific volume and hydration, *Biophys. J.* **91**, (2006) 1591–1603.
6. B. Alpert, G. Beylkin, R. Coifman and V. Rokhlin, Wavelet-like bases for the fast solution of second-kind integral equations, *SIAM J. Sci. Comp.* **14** (1993) 159–184.
7. P.M. Anselone, *Collectively compact operator approximation theory and applications to integral equations,* Prentice-Hall, Englewood Cliffs, NJ (1971).

8. P.M. Anselone, Singularity subtraction in the numerical solution of integral equations, *J. Austral. Math. Soc. (Series B)* **22** (1981) 408–418.

9. K.E. Atkinson, The numerical solution of Laplace's equation in three dimensions, *SIAM J. Num. Anal.* **19** (1982) 263–274.

10. K.E. Atkinson, *The numerical solution of integral equations of the second kind,* Cambridge University Press (1997).

11. C. Brebbia, J. Telles and L. Wrobel, *Boundary element techniques,* Springer-Verlag (1984).

12. J.P. Brody and P. Yager and R.E. Goldstein and R.H. Austin, Biotechnology at low Reynolds numbers, *Biophysical J.* **71** (1996) 3430–3441.

13. J.P. Brody and P. Yager, Diffusion-based extraction in a microfabricated device, *Sensors and Actuators A* **58** (1997) 13–18.

14. D. Brune and S. Kim, Predicting protein diffusion coefficients, *Proc. Natl. Acad. Sci. USA* **90** (1993) 3835–3839.

15. O.P. Bruno and L.A. Kunyansky, A fast, high-order algorithm for the solution of surface scattering problems: basic implementation, tests and applications, *J. Comp. Phys.* **169** (2001) 80–110.

16. L.F. Canino and J.J. Ottusch and M.A. Stalzer and J.L. Visher and S.M. Wandzura, Numerical solution of the Helmholtz equation in 2D and 3D using a high-order Nyström discretization, *J. Comp. Phys.* **146** (1998) 627–663.

17. C.R. Cantor and P.R. Schimmel, *Biophysical chemistry, Part II*, W.H. Freeman Publishing (1980).

18. G. Chen and J. Zhou, *Boundary element methods,* Academic Press (1992).

19. C.-F. Chou and O. Bakajin and S.W.P. Turner and T.A.J. Duke and S.S. Chan and E.C. Cox and H.G. Craighead and R.H. Austin, Sorting by diffusion: An asymmetric obstacle course for continuous molecular separation, *Proc. Natl. Acad. Sci. USA* **96** (1999) 13762–13765.

20. H.-P. Chou and M.A. Unger and S.R. Quake, A microfabricated rotary pump, *Biomed. Microdevices* **3** (2001) 323–330.

21. T.A.J. Duke and R.H. Austin, Microfabricated sieve for the continuous sorting of macromolecules, *Phys. Rev. Lett.* **80** (1998) 1552–1555.

22. R. Finn, On the exterior stationary problem for the Navier-Stokes equations and associated perturbation problems, *Arch. Rat. Mech. Anal.* **19** (1965) 363–406.

23. M. Ganesh, I.G. Graham and J. Sivaloganathan, A new spectral boundary integral collocation method for three-dimensional potential problems, *SIAM J. Num. Anal.* **35** (1998) 778–805.

24. M.A. Goldberg and C.S. Chen, *Discrete projection methods for integral equations,* Computational Mechanics Publications (1997).

25. O. Gonzalez and J. Li, Modeling the sequence-dependent diffusion coefficients of short DNA sequences, *J. Chem. Phys.* **129** (2008) 165105.

26. O. Gonzalez, On stable, complete and singularity-free boundary integral formulations of exterior Stokes flow, *SIAM J. Appl. Math.* **69** (2009) 933–958.

27. O. Gonzalez and J. Li, On the hydrodynamic diffusion of rigid particles of arbitrary shape with application to DNA, *SIAM J. Appl. Math.* **70** (2010) 2627–2651.

28. O. Gonzalez and J. Li, A convergence theorem for a class of Nyström methods for weakly singular integral equations on surfaces in $\mathbb{R}^3$, *submitted*, arXiv:1205.5064.

29. I.G. Graham and I.H. Sloan, Fully discrete spectral boundary integral methods for Helmholtz problems on smooth closed surfaces in $\mathbb{R}^3$, *Numer. Math.* **92** (2002) 289–323.

30. N.M. Günter, *Potential theory,* Frederick Ungar Publishing (1967).

31. F.K. Hebeker, A boundary element method for Stokes equations in 3-D exterior domains, in *The Mathematics of Finite Elements and Applications V*, Edited by J.R. Whiteman, (1985) 257–263.

32. G.C. Hsiao and W.L. Wendland, *Boundary integral equations,* Applied Mathematical Sciences, Volume 164, Springer-Verlag (2008).

33. J.G. Heywood, On uniqueness questions in the theory of viscous flow, *Acta Math.* **136** (1976) 61–102.

34. A.E. Kamholz and B.H. Weigl and B.A. Finlayson and P. Yager, Quantitative analysis of molecular interaction in a microfluidic channel: The T-Sensor, *Anal. Chem.* **71** (1999) 5340–5347.

35. S. Kim and S.J. Karrila, *Microhydrodynamics,* Butterworth-Heinemann Publishing (1991).

36. R. Kress, *Linear integral equations,* Applied Mathematical Sciences, Volume 82, Springer-Verlag (1989).

37. L.V. Kantorovich and V.I. Krylov, *Approximate methods of higher analysis,* Interscience (1958).
38. L.A. Kunyansky and O.P Bruno, A fast, high-order algorithm for the solution of surface scattering problems II: Theoretical considerations, *submitted.*
39. A. Kurganov and J. Rauch, The order of accuracy of quadrature formulae for periodic functions, in *Progress in nonlinear differential equations and their applications*, Volume 78, A. Bove, D. Del Santo and M.K.V. Murthy, Eds., Birkhäuser (2009) 155–159.
40. O.A. Ladyzhenskaya, *The mathematical theory of viscous incompressible flow,* Revised English Edition, Gordon and Breach (1963).
41. C. Lage and C. Schwab, Wavelet Galerkin algorithms for boundary integral equations, *SIAM J. Sci. Comp.* **20** (1999) 2195–2222.
42. S.L. Levy and H.G. Craighead, DNA manipulation, sorting, and mapping in nanofluidic systems, *Chem. Soc. Rev.* **39**, (2010) 1133–1152.
43. J. Li, *A computational model for the diffusion coefficients of DNA with applications*, Ph.D. dissertation, The University of Texas at Austin (2010).
44. P.A. Martin, *Multiple scattering,* Encyclopedia of Mathematics and its Applications, Volume 107, Cambridge University Press (2006).
45. R.J. Meagher and J.-I. Won and L.C. McCormick and S. Nedelcu and M.M. Bertrand and J.L. Bertram and G. Drouin and A.E. Barron and G.W. Slater, End-labeled free-solution electrophoresis of DNA, *Electrophoresis* **26** (2005) 331–350.
46. R.J. Meagher and J.-I. Won and J.A. Coyne and J. Lin and A.E. Barron, Sequencing of DNA by free-solution capillary electrophoresis using a genetically engineered protein polymer drag-tag, *Anal. Chem.* **80** (2008) 2842–2848.
47. S.G. Mikhlin, *Linear integral equations,* International Monographs on Advanced Mathematics and Physics, Hindustan Publishing Corporation (1960).
48. S.G. Mikhlin, *Multidimensional singular integrals and integral equations,* International Series of Monographs in Pure and Applied Mathematics, Volume 83, Pergamon Press (1965).
49. S.G. Mikhlin and S. Prössdorf, *Singular integral operators,* Springer-Verlag (1986).
50. F.K.G. Odqvist, Über die randwertaufgaben der hydrodynamik zäher flüssigkeiten, *Math. Zeit.* **32** (1930) 329–375.
51. B. O'Neill, *Elementary differential geometry,* Academic Press (1966).
52. H. Power and G. Miranda, Second kind integral equation formulation of Stokes' flows past a particle of arbitrary shape, *SIAM J. Appl. Math.* **47** (1987) 689–698.
53. H. Power and L.C. Wrobel, *Boundary integral methods in fluid mechanics,* Computational Mechanics Publications (1995).
54. C. Pozrikidis, *Boundary integral and singularity methods for linearized viscous flow,* Cambridge University Press (1992).
55. S.R. Quake and A. Scherer, From micro- to nano-fabrication with soft materials, *Science* **290** (2000) 1536–1540.
56. A. Rathsfeld, Quadrature methods for 2D and 3D problems, *J. Comp. Appl. Math.* **125** (2000) 439–460.
57. E.A. Schilling and A.E. Kamholz and P. Yager, Cell lysis and protein extraction in a microfluidic device with detection by a fluorogenic enzyme assay, *Anal. Chem.* **74** (2002) 1798–1804.
58. T.M. Squires and S.R. Quake, Microfluidics: Fluid physics at the nanoliter scale, *Rev. Mod. Phys.* **77** (2005) 977–1026.
59. H.A. Stone and S. Kim, Microfluidics: Basic issues, applications, and challenges, *AIChE J.* **47** (2001) 1250–1254.
60. C. Tanford, *Physical chemistry of macromolecules*, Wiley (1961).
61. J. Tausch and J. White, Multiscale bases for the sparse representation of boundary integral operators on complex geometry, *SIAM J. Sci. Comp.* **24** (2003) 1610–1629.
62. G.M. Whitesides and A.D. Strook, Flexible methods for microfluidics, *Phys. Today* **54** (2001) 42–48.
63. H. Yamakawa, *Modern theory of polymer solutions*, Harper & Row (1971).
64. L. Ying, G. Biros and D. Zorin, A high-order 3D boundary integral equation solver for elliptic PDEs in smooth domains, *J. Comp. Phys.* **219** (2006) 247–275.